Planar Investigation of a CobraMRV Reentry Flowfield Using Pulse-Burst, Cross-Correlation DGV

Ross A. Burns[1]
National Institute of Aerospace, Hampton, VA, 23666, USA

and

Timothy W. Fahringer, Jr.[2] and Paul M. Danehy[3]
NASA Langley Research Center, Hampton, VA, 23681, USA

The flowfield around a Co-Optimization Blunt-body Reentry Analysis Mid-lift/drag-ratio Rigid Vehicle (CobraMRV) vehicle is investigated with a combination of high-speed planar laser Mie scattering (PLMS) and pulse-burst cross-correlation Doppler global velocimetry (PB-CC-DGV). Tests were conducted in the NASA Langley 4-foot Supersonic Unitary Plan Wind Tunnel (UPWT) over a range of different tunnel operating conditions and model configurations. Results indicate a complex shock-boundary layer interaction. Scalar information extracted from the PLMS show the evolution of the bow shock structure, while streamwise velocity measurements indicate the spatial evolution of the shock-boundary layer interaction including the growth of the separation shock foot and eventual reacceleration of the flow at farther downstream locations. Assessment of multiple cases show strong Mach and Reynolds numbers driven effects on the character of the shock-boundary layer interactions. Measurement uncertainties ranged from 50 to 150 m/s throughout the region of interest, driven largely by angular uncertainties and instabilities in the laser pointing. The mean accuracy of the freestream measurements was found to be 5.2-percent of tunnel predicted values.

I. Nomenclature

Ordinates

x	=	Tunnel streamwise direction [m]
y	=	Tunnel vertical direction [m]
z	=	Tunnel spanwise direction [m]
s	=	Sheetwise direction [m]
x_m	=	Model centroid x-position [in.]
x_{px}	=	Image horizontal direction [px]
y_{px}	=	Image vertical direction [px]

Angles

ϵ	=	Error
ρ	=	Pearson correlation coefficient
λ	=	Wavelength [nm]
$\Delta\nu$	=	Doppler shift [MHz, GHz]

Vectors

$\hat{\imath}$	=	Laser incidence vector
$\hat{o}$	=	Observation vector
$\vec{u}$	=	Velocity [m/s]

[1] Research Engineer, Advanced Measurement and Data Systems Branch.
[2] Lead Research AST, Advanced Measurement and Data Systems Branch, AIAA Member.
[3] Senior Technologist for Advanced Measurement Systems, Advanced Measurement and Data Systems Branch, AIAA Associate Fellow.

θ	=	Polar angle [°]
ϕ	=	Azimuthal angle [°]
ψ	=	Roll angle [°]

Symbols

c	=	Coefficient
f	=	Focal length [m,mm]
k	=	Radial distortion coefficient [m^{-2}]
l	=	Length, plane to lens [m]
os	=	Offset [px]
δ	=	Uncertainty

Subscripts

c	=	Camera
$\hat{\imath}$	=	Associated with $\hat{\imath}$
$\hat{o}$	=	Associated with $\hat{o}$
ref	=	Reference channel
sig	=	Signal channel
x	=	x-component
y	=	y-component
z	=	z-component

II. Introduction

The collective ability of the aerospace industry to accurately simulate complex flowfields has grown considerably over the past decade.[1] With the growing availability of computational resources, improved simulation methodologies, and more advanced multidisciplinary research efforts, the question of the utility of large-scale, ground-test facilities grows more relevant with every passing year, both as an issue of necessity and of cost. In light of the NASA CFD 2030 Vision, such questions will likely be asked with increasing frequency in the coming years. One effort currently underway to examine the feasibility of retiring a well-used experimental facility is taking place at NASA Langley Research Center's 4-foot Supersonic Unitary Plan Wind Tunnel (UPWT).[2] This facility is storied for its contributions to the Entry, Descent, and Landing (EDL) experimental aerothermodynamics at NASA Langley.[3] In these tests, full wind tunnel simulations modeling the plenum through the full extent of the test section are being directly compared with experimentally obtained measurements in these flowfields to assess overall predictive capabilities, as well as cost analyses.[4] In addition to empty-test-section evaluations, these studies are also looking to examine the flowfield around a co-optimization blunt-body reentry analysis mid-lift-to-drag-ratio rigid vehicle (CobraMRV), a conceptual, fully parametrized and optimized, mid lift/drag reentry vehicle intended for Mars atmospheric entry.[5] Included in these comparisons is not simply qualitative assessment of flow features, but a wide array of quantitative comparisons including integrated force and moment measurements, surface pressure measurements, and flow angularity, among others.

The present studies, in conjunction with a series of other experimental endeavors, seek to create an extensive database for the validation of representative simulations of CobraMRV flowfields within the UPWT. The off-body flowfield measurements described in this paper consist of two measurement techniques, high-speed planar laser Mie scattering (PLMS) and pulse-burst, cross-correlation, Doppler global velocimetry (PB-CC-DGV). High-speed PLMS measurements provide a qualitative view of primary flowfield structures, such as shockwaves, as well as unsteady structures that may be present in the tunnel freestream. PB-CC-DGV is a novel velocimetry technique, which uses a pulse-burst laser with rapid frequency scanning to resolve a Doppler shifted absorption spectra.[6] This technique is similar in operation principle to the original cross-correlation Doppler global velocimetry,[7] and has been used previously within the UPWT facility to some success, measuring the velocity change across a weak oblique shock to approximately 1-percent accuracies.[8] These studies also aim to expand on that previous work to make practical, large field-of-view (FOV) measurements. This paper is organized as follows: after the introduction, the experimental systems and analytical methods are described. A full data set is presented along with some collected results from multiple runs. A detailed uncertainty analysis is presented in the Appendix.

III. Measurement Background and Description

The data and experimental methods herein described are part of a broader experimental effort to assess the quality of computational fluid dynamic (CFD) simulations of the 4-foot Supersonic Unitary Plan Wind Tunnel (UPWT), and to determine, in part, whether simulations are yet of sufficient fidelity to forego use of the experimental facility. These measurements specifically sought to examine the shockwave-turbulent boundary layer interaction (SWTBLI) beneath a scale model of a CobraMRV. Selection of this region of interest was made based on recommendations from previous testing. It was noted in the tests immediately preceding these that the shock-induced heating of the gas following the bow shock would cause melting/evaporation/sublimation of the ice crystals used as a seeding medium, and thus

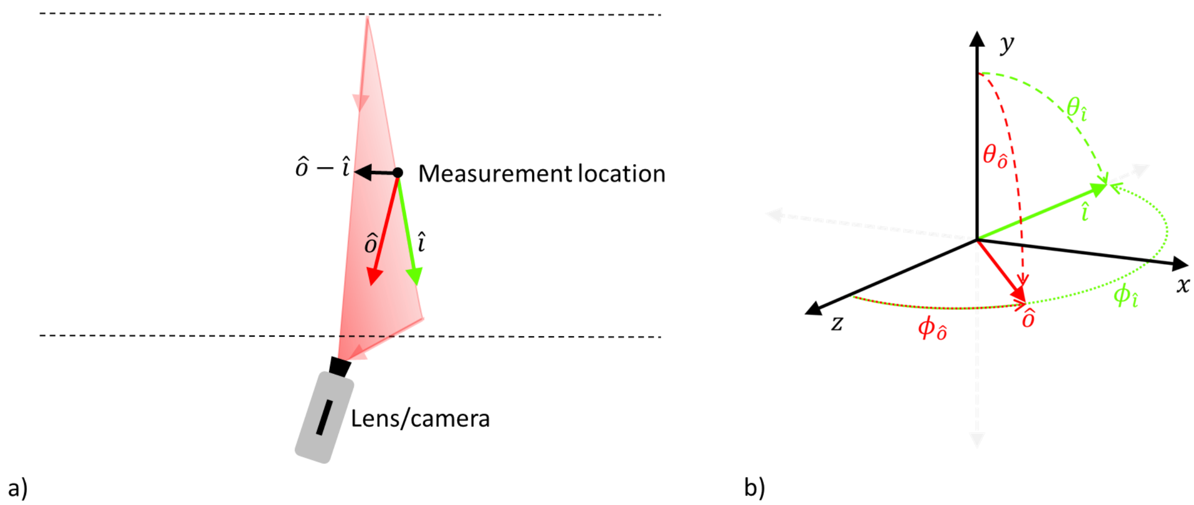

Figure 1. Relevant design vector orientations for the CobraMRV experiments. a) Overhead view of vector orientation and b) vector diagram used at each measurement location showing relevant angles. Dashed lines in a) represent the boundaries of the wind tunnel.

examination of the near-body or wake structures was not likely to succeed. The decision was thus made to examine SWTBLI region, which is also quite difficult to predict with present day simulations.

The selection of experimental techniques for these studies was done to maximize the amount of information that could be provided to the customers and simultaneously maximize the likelihood of (at least) partial success during the experiments. Based on previous testing, the appropriate candidate for planar velocimetry was the pulse-burst, cross-correlation Doppler global velocimetry (PB-CC-DGV) technique.[6] While difficult to implement and analyze, a previous (albeit simpler) application of PB-CC-DGV in the UPWT produced accurate velocimetry, though over a relatively small field of view (FOV).[8] Other particle-based techniques (e.g., particle image velocimetry or laser Doppler velocimetry), that rely on external seeding systems not available in the facility, or molecular techniques (e.g., molecular tagging velocimetry), that often require specialized seeding systems and UV-grade windows, were not practically viable, so the selection of PB-CC-DGV was viewed as the best alternative. However, the general difficulty in implementing this technique was concerning, and the additional complication of observing a large field of view (specifically, as much of the span of the tunnel as was possible), which had not been attempted previously with this technique further reduced the likelihood of success for obtaining quantitative velocity data in these tests. The only technique which had successfully applied in this facility to a large FOV was planar laser Mie scattering (PLMS), which had been conducted on two separate instances and was able to provide time-resolved, instantaneous images of flow structures over large areas.[9] It was thus decided that the experiments would focus on providing PLMS data for the regions of interest. However, while planning for the experiments, a breakthrough in the optical design (see Section IV.C.5) enabled the *possibility* of PB-CC-DGV without significantly hindering the acquisition of PLMS. Since PB-CC-DGV utilizes the same basic data type as PLMS, simultaneous acquisition of high-speed PLMS and mean velocity measurements was thus possible pending practical difficulties and experimental complications. This paper specifically focuses on the velocimetry analysis of the data acquired in this experiment, documenting the experimental methods, data analysis methods, and measurement uncertainties. Recommendations for improvement are also provided.

PB-CC-DGV is a generational variant of the Doppler global velocimetry technique, which is used to infer velocity through the measurement of luminal Doppler shifts. A complete description of the technique can be found in Refs. 6 through 8. PB-CC-DGV utilizes a pulse-burst laser with a frequency-scanning oscillator. During a laser burst, the laser frequency is scanned across an absorption feature of (typically) a molecular optical filter, and the resulting optical transmission is used to measure a full Doppler-shifted absorption spectrum at each pixel. Unlike traditional Doppler global velocimetry, which has also seen success in this facility, [10] the CC-DGV method [7] used herein is resistant to errors induced by random sources (background scatter, spatial/temporal fluctuations in laser intensity). By further comparison with a zero-velocity reference, the Doppler shift ($\Delta\nu$) at each pixel is determined. Spatial calibration of the data can be used to ascertain information about the velocity field. Equations 1.1 and 1.2 describe the relationship between the velocity, Doppler shift, and measurement geometry:

$$\Delta\nu = \frac{\vec{u} \cdot (\hat{o} - \hat{\imath})}{\lambda} \quad (1.1)$$

$$\Delta\nu = \frac{u_x(\hat{o} - \hat{\imath})_x + u_y(\hat{o} - \hat{\imath})_y + u_z(\hat{o} - \hat{\imath})_z}{\lambda} \quad (1.2)$$

In Eqs. 1, $\vec{u}$ is the vector velocity, $(\hat{o} - \hat{\imath})$ is the measurement sensitivity vector (effectively, the directional component of velocity that is measured), and λ is the laser (center) wavelength during the scan. For a complete evaluation of the velocity, at least 3 independent measurements of Doppler shift (at different measurement angles) must be made. However, judicious design of the optical system can be used to simplify the measurement process and/or extract specific velocity components. Figure 1a shows a basic layout (overhead) of the experimental geometry from these CobraMRV tests. The sensitivity vector is the difference between two unit-vectors, the observation vector ($\hat{o}$) and the laser incidence vector ($\hat{\imath}$). The observation vector points from the measurement location back toward the camera, while the laser incidence vector points in the direction of laser propagation. A vector diagram showing the relevant angles is given in Fig. 1b, notably the azimuthal (ϕ) and polar (θ) angles. The origin of this sub-coordinate system is at the measurement location itself.

These experiments were designed to primarily measure the streamwise (x-) component of velocity. To achieve this effect, the experiment was set up so that the camera and laser were oriented at nearly the same (but opposite) angles with respect to the tunnel y-z plane. With this setup, along the centerline of the camera's optical axis the y- and z-components of the observation and incidence vectors are of the same direction and magnitude and thus cancel out in the sensitivity vector. Thus, in these areas the measured Doppler shift is principally sensitive to the x-component of velocity, and the velocity can be evaluated as:

$$u_x = \frac{\lambda\Delta\nu}{(\hat{o} - \hat{\imath})_x} \quad (2)$$

The flow is principally oriented in the streamwise direction over most of the region of interest, and consequently the application of Eq. 2 would be an accurate estimate of the streamwise velocity. However, since the extent to which the flow is so oriented cannot be ascertained from these measurements alone, Eq. 2 is only truly valid in regions where the sensitivity vector is primarily streamwise. For this reason, it is important to remember that simulations can be compared either (or both) to the streamwise velocity and/or Doppler shift. Equation (1.2) can be used with the full velocity vector in a simulation to evaluate the intended Doppler shift, which can be directly compared to the measurement. The advantage of comparing computational simulations with measured Doppler shift is that errors associated with assumptions involved with using Eq. 2 are eliminated.

IV. Experimental Methods

This section describes all aspects of the experimental setup and procedures.

A. Test Facility

The tests were conducted in the 4-Foot Supersonic Unitary Plan Wind Tunnel (UPWT). The Mach number of the facility is continuously variable from 1.47 to 4.64, achieved by utilizing a sliding nozzle block configuration. Two different test sections account for the full range of Mach numbers: Test Section I covers Mach numbers in the range of 1.47 to 2.87, while Test Section II accommodates Mach numbers ranging from 2.29 to 4.64. These tests were conducted in Test Section II. Test section II has cross-sectional dimensions of 1.32 m (H) by 1.22 m (W) and an overall length of 2.14 m. Test conditions varied for each test case. The flow was seeded for flow visualization and DGV by injecting liquid water downstream of the test section. In circulating through the facility, a fog of ice crystals develops in the nozzle and passes into the test section; this fog was used as the scattering medium. Note that this fog has been used in previous DGV and flow visualization experiments,[10,11] and the particles that comprise the fog are generally too small for performing PIV. The tunnel dew point was maintained between 276.6 K (38 °F) and 291.5 K (65 °F) to maintain the desired level of seeding, with higher values being used at higher Mach number operation. It was observed in post-test analysis that the force and moment measurements on the model were modified slightly (a few percent) by the presence of the water vapor. During testing, a higher seed concentration was chosen in order to minimize the laser-pulse energy used and thus reduce the risk of damaging the facility windows. In future experiments, the balance between these parameters could be redressed to limit the effects of the measurement on the flowfield without significantly compromising the safety of the facility.

Optical access to the test section was afforded by a series of vertical windows arranged along each sidewall. Each window was approximately 130 mm wide and separated from the next by a 30 mm steel spar, each of which was approximately 230 mm deep. These windows can be seen in the test section diagram in Fig. 2, along with the test section optics, camera configuration, and model position. Note also in Fig. 2 the orientation of the coordinate system. The x-direction is the streamwise direction with its origin at the beginning of the test section, the y-direction is the vertical direction (positive pointing up), and the z-direction is the tunnel spanwise direction (z = 0 is the spanwise center of the tunnel). The origin of the y-direction is nominally the vertical center of the tunnel, but has been repositioned to the floor of the tunnel for this report since the region of interest is the SWTBLI. Also note that an additional coordinate is used in this report, the s-direction or sheetwise direction. The sheetwise direction is oriented along the direction of the laser sheet, with its center at the spanwise center of the tunnel. The s-direction is very similar in orientation to the z-direction but is tilted at a slight angle (about 2.2°) about the y-axis; it is a convenience for the presentation of and understanding the data.

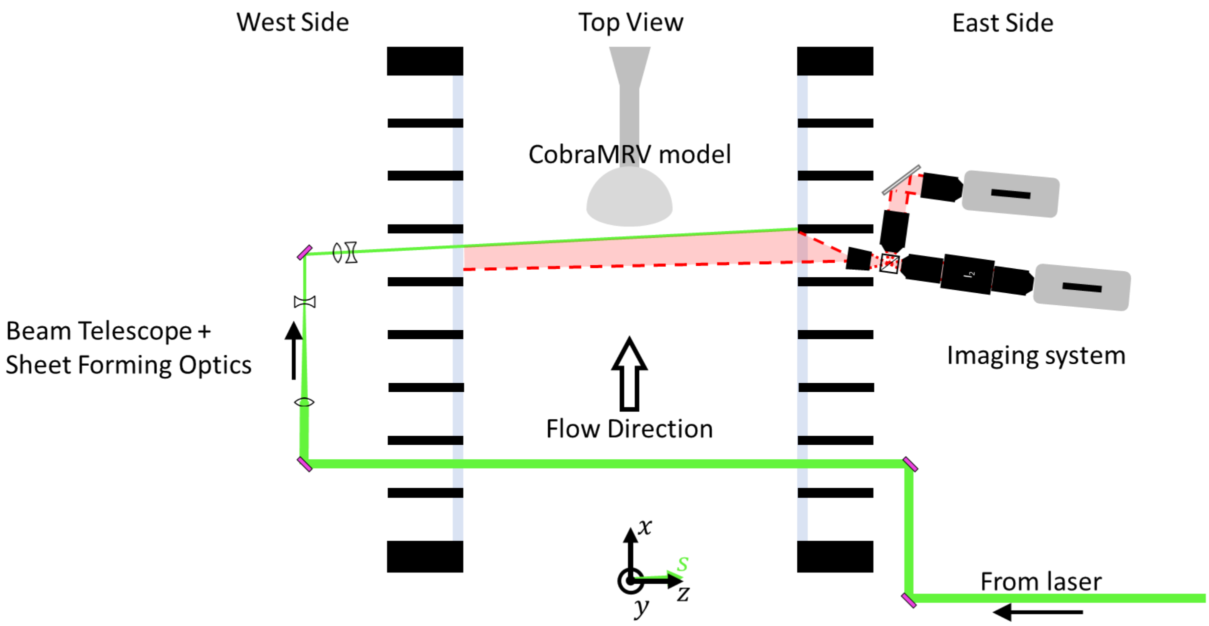

Figure 2. Top-view diagram of UPWT test section with CobraMRV model and major optical components. A detailed diagram of the imaging system can be found Figure 5a.

B. Test Article

A rendering of the CobraMRV model is shown in Fig. 3; this model consisted of an oblong central body approximately 380 mm long by 160 mm wide in dimension affixed to the tunnel sting assembly. The model had a nominal angle of attack (AoA) of 55°, and all three major angles (roll, pitch, and yaw) could be adjusted using the sting assembly. The AoA of the model could be varied from 41° through 70° with this method. Additionally, the model could be axially translated through the wind tunnel over a distance of 0.75 m. The CobraMRV also had interchangeable control fins that allowed the fin angle to be statically adjusted. Flap angles (F/A) of 0° (flush with body as shown in Fig. 3) and 35° were used during the testing with laser visualization and velocimetry. In characterizing the position of the model, the nominal model position is noted as x_m = 0.88 m (34.75 in.), corresponding to the model center of gravity used in other experimental campaigns. During testing, in order to tomographically examine the flowfields being studied, the model was translated through the wind tunnel in 25.4 mm (1-in.) increments. In reconstructing data during analysis, the model positions have been converted into notional tunnel positions with the model located at the nominal position. This conversion was done so that flow features appearing in different runs with different model beginning and end points can be viewed from a common frame of reference.

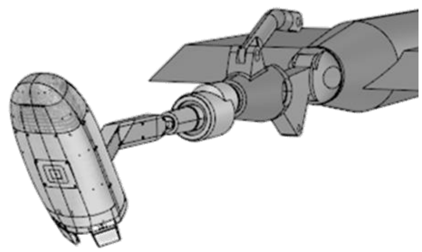

Figure 3. Rendering of CobraMRV model attached to tunnel sting assembly.

C. Optical Systems

1. Laser system

The laser used in these studies was a burst-mode, master oscillator, pulsed amplifier system (Spectral Energies QuasiModo). The laser utilized an external cavity diode laser (ECDL, Sacher LiON series) as a seed laser, which allowed the laser frequency to be rapidly scanned through variation of the laser diode current or through piezo actuation. The operating frequency of the laser was set to 100 kHz, while the burst duration and period were 10 ms and 12 s, respectively. The second harmonic of this Nd:YAG system was used with the center wavelength set to 532.217 nm to capture the desired I_2 absorption features. The laser linewidth is specified between 60 and 100 MHz, and a pulse duration of 20 ns was used. Figure 4 presents a diagram of the primary laser system. The output from the main amplifier head is divided into two pathways: a diagnostic leg and the main experimental leg. The diagnostic leg, which was sampled by taking the small fraction of light that passed through a high-reflectivity mirror, housed the diagnostic systems used to characterize the laser output. The main experimental leg first passed through a variable attenuator ($\lambda/2$-plate and plate polarizer) and then a one-to-three inverting telescope with a small (500 μm) iris at its focus, which was used to help limit beam steering associated with thermal lensing during the burst and to expand the beam diameter. This portion of the laser system then transmitted the beam over to the wind tunnel test section. The laser was operated at full power at all times, and the energy content of the beam was controlled exclusively with the variable attenuator. While a similar effect could be achieved by adjusting amplifier voltages within the laser, doing so would have made both the spatial profile of the beam and the temporal profile of each burst more variable and unpredictable.

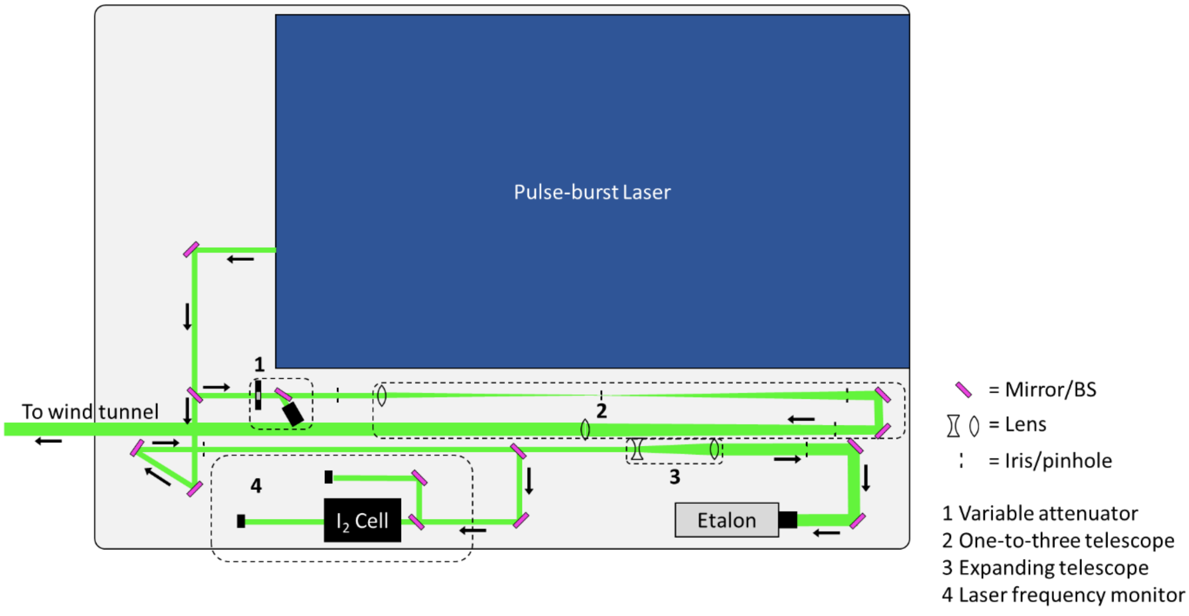

Figure 4. Diagram of primary laser setup.

2. Laser frequency monitor (LFM)

The LFM acted as a zero-velocity reference for comparison with Doppler-shifted spectra. The device allowed an instantaneous measurement of optical absorption. The LFM consisted of two photodiodes (Thorlabs DET210), each fitted with an identical laser line filter (1 nm FWHM, passing 532 nm) and a lens / optical diffuser system to minimize the effects of spatial variations in the laser profile or position. The laser beam in the diagnostics leg (containing less than one percent of the total laser energy) is sampled using two partially reflective mirrors, one 20-percent and one 50-percent, to reduce the overall input energy to the LFM. This input energy is divided into two paths using a nonpolarizing 50-percent beam-splitter, each path leading to one photodiode. One path propagates unperturbed, while the other passes through a gaseous I_2 cell (ISSI I2M-5, cell pressure 1 Torr at 40 °C), which was held at a constant 70 °C by a thermoelectric controller (Digi-Sense TC5000). The overall intensity of the laser was adjusted by placing absorptive neutral-density (ND) filters on the front of the system, while the balance of the channels was accomplished by placing lower-density ND filters on each path. The beam paths of the LFM system were enclosed in one-inch diameter threaded-tube-system components to prevent contamination from background scattered light. The output from the photodiodes was captured using an oscilloscope (Tektronix DPO7354) with custom data acquisition software to automatically acquire the traces from multiple sequential bursts, allowing the system to run for 10s of minutes without user input.

3. Laser etalon

A confocal Fabry-Pérot etalon (Burleigh) with a free-spectral range of 750 MHz was used to monitor relative changes in the laser frequency. In combination with the LFM, the etalon allowed the zero-velocity absorption spectra to be correctly scaled in the frequency domain and corrected for errors associated with nonlinear scanning. The input to the etalon from the diagnostic leg of the laser system was diametrically expanded by a factor of 6 using a telescopic lens pair (-50-mm and +300-mm spherical lenses) and attenuated using absorptive ND filters to adjust the intensity prior to entering the etalon. Data from the etalon were acquired using the same 4-channel oscilloscope as the LFM. Note that the fourth channel of the oscilloscope was used for one of several system inputs such as the waveform input to the ECDL, one camera's exposure positive signal, or the current out of the ECDL, depending on what was needed at the time.

4. Test-section optics

A diagram of the test-section optics can be found in Fig. 2. After receiving the beam on the east side of the test section, the beam was initially rotated (90°) using an orthogonal pair of high-reflectivity mirrors. The beam was then transmitted through the upstream end of the test section to the opposite (west) side of the wind tunnel facility. A converging telescopic lens pair (+300-mm and -100-mm spherical lenses) was positioned next in the optical path; the distance between these lenses was set to be slightly ahead of the point of collimation to allow the beam to focus gently at the center of the test section, acting as the focusing lens of the sheet forming optics. After this telescope, the beam was passed through a cylindrical lens-doublet (+25.4-mm and -37.5-mm cylindrical) to expand it into a large, vertically-oriented sheet (> 0.75 m tall). The expanding sheet was routed into the test section at a shallow angle and directed onto one of the steel spars on the east side of the test section, which acted as a beam stop during data acquisition. As a consequence, a small amount of laser scatter was visible on most metal surfaces imaged by the cameras. The decision to orient the laser sheet in this manner was made to increase the scattering intensity using forward scatter, thus limiting the laser-pulse energy required for the measurement. Because of the size and weight of the imaging system described in the subsequent section that required the optical mounting surfaces on the East side of the tunnel, routing the beam across the test section was a practical necessity and was also the shortest available beam path to achieve the desired experimental configuration.

5. Dual-Relay Imaging System (DRIS)

These experiments utilized a new dual-relay imaging system (DRIS) to enable the simultaneous acquisition of both PLMS and PB-CC-DGV data. A schematic of this optical system is shown in Fig. 5a. Previous experiments utilizing PB-CC-DGV utilized a single, large plate beam-splitter to divide the signal between two different cameras. In these experiments, however, the desired FOV was approximately 100 times the area of that in previous experiments and required faster (shorter focal length) imaging lenses. Additionally, the desired FOV necessitated the placement of the lens between two of the test-section spars, making the same dual-viewing system used in previous tests both impractical and impossible. Thus, a new dual-view system was developed that took advantage of imaging relays to overcome the spatial constraints of the experiment. The DRIS utilized a single imaging lens (35-mm, $f/1.2$); this lens was mounted between the spars on the East side of the test section as shown in Fig. 2. The light collected from this lens was projected onto a non-polarizing beam-splitter cube (50%); the image plane was located near the front surface of this beam-splitter. Following the beam-splitter, two relay lenses (150-mm macro lenses, $f/2.8$) were positioned in reverse such that the nominal image planes were coincident with that of the primary imaging lens. On one path (right leg of Fig. 5a), the light passing through the first relay lens reflected off a flat mirror before entering a second, identical lens. This lens was connected to a high-speed CMOS camera (Photron FASTCAM SA-Z) by a custom-made Scheimpflug mount. The other leg of the DRIS (left path in Fig. 5a) was instead directed through a gaseous iodine cell (identical to the one in the LFM) before entering the second relay lens. The second relay lens on this path was similarly connected to a high-speed CMOS camera (Photron FASTCAM SA-Z) with a Scheimpflug mount. The front-to-front separation between both sets of relay lenses was approximately 180 mm.

In these experiments, high-speed PLMS data were acquired through the right leg of the DRIS, which will be referred to as the 'reference' channel. The camera was operated at 25 kHz in order for the cameras to have almost their full fields of view (1024 px by 768 pixels), and captured 1 of every 4 laser pulses. The decision to operate the camera and laser and different repetition rates was made to limit the laser-pulse energy and give finer control over the laser-burst energy with the variable attenuator. The PB-CC-DGV data utilized both paths of the DRIS; the left leg will be referred to as the 'signal' channel throughout. This channel contained the iodine cell required for CC-DGV (identical size and fill conditions described with the LFM previously), and the camera on that path was synchronized with the reference channel, also acquiring images at 25 kHz. The exposure-out signal from the reference channel camera was sent to the same oscilloscope used for the LFM and etalon for data acquisition. A burst of roughly 300 images was acquired by both cameras during each 10.5 msec laser burst. The DRIS FOV relative to the laser sheet and test section are shown in Fig. 5b.

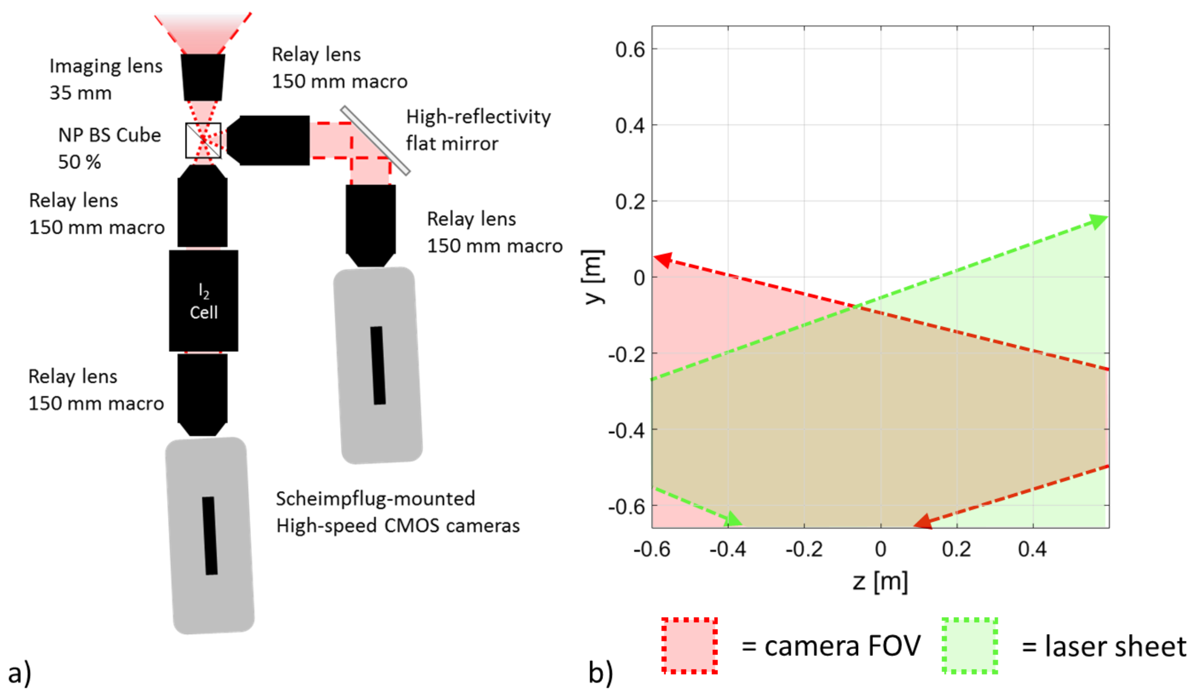

Figure 5. Schematic of dual-relay imaging system used in the CobraMRV measurements (a) and the associated field-of-view with respect to the laser sheet and test section (b).

D. Test Matrix

Table 1 shows the complete matrix of test conditions and model configurations used during the CobraMRV tests. The results that follow in Section VI are taken from Case 5. Selected data from other cases are presented as well.

Table 1: Complete test matrix for PB-CC-DGV COBRA MRV studies

Case #	Mach #	Re # [$\times 10^6$/ft]	To [°F]	AoA [°]	F/A [°]	Scan Range [in.]
Test	2.399	3.0	125	55	0/0	25 – 55
1	2.399	3.0	125	55	0/0	37 – 55
2	2.399	3.0	125	41	0/0	37 – 55
3	2.404	4.5	150	55	0/0	37 – 55
4	3.477	1.0	125	55	0/0	32 – 50
5	3.500	3.0	125	55	0/0	32 – 50
6	3.507	4.5	150	55	0/0	32 – 50
7	4.631	3.0	150	55	0/0	30 – 48
8	2.399	3.0	125	55	35/35	37 – 52
9	3.500	3.0	125	41	35/35	32 – 53
10	4.631	3.0	150	55	35/35	30 – 48
11	2.399	3.0	125	55	35/35	37 – 52
12	3.500	3.0	125	55	35/35	32 – 53

V. Data Analysis

This section contains an in-depth description of all steps of data processing and analysis. Data analysis was done one burst at a time. Prior to any data analysis, all bursts of data were visually checked to ensure that 1) the reference and signal channels of the imaging system matched (correctly numbered), 2) no mode hops were observed in the seed laser, and 3) no fixed pattern noise was observed. Of roughly 2600 bursts of data collected during testing, 18 burst-pairs were affected by incorrect numbering, 7 by laser mode-hops, and no fixed pattern noise that was consistent with previous test entries was observed. Incorrect numbering errors were corrected if possible, while observed mode-hops were not analyzed due to the incorrect position of the absorption well in the frequency scan.

A particularly challenging element of the data analysis that follows, in terms of adapting previous versions of this same data analysis to the current data set, was the seemingly incorrect placement of the dotcard calibration target used during data acquisition. This error was discovered several months after the tests had concluded when the nominally dewarped images retained significant asymmetries that couldn't be explained through physical or analytical mechanisms. It is not clear exactly how this error occurred; the alignment laser beam was well-aligned with the high-power beam during each day's setup, and the alignment beam was also visibly coincident with the calibration target. It is likely that the laser beam grossly adjusted its position as the system warmed up (after the calibration images were acquired). Furthermore, there are sufficient laser position fluctuations present within each burst and between bursts that miscalibration can be visibly detected if observed in sequence. These conditions were all exacerbated by the imaging configuration (which had a severe angle between the laser sheet and camera views) and particularly long beam path used during these experiments. Because of these revelations, as well as the sizeable quantity of data collected, the entire data analysis procedure used previously (see Ref. 8) had to be remade not only to attempt to correct this particular error, but to optimize all steps of analysis to function more efficiently in both parallelized and vectorized processing formats.

A. Image Mapping

After importing the raw camera data, the first step in the analytical process was image mapping. Image mapping is a process whereby the two camera channels (reference and signal) are mapped pixel-by-pixel onto a common coordinate system. Under normal circumstances, image mapping is achieved by using a calibration target (dot card, checkerboard, or other) to find common locations between the two camera channels. However, since the calibration target was found to have been improperly positioned during the experiments, an alternative approach had to be employed that used flow features observed in the instantaneous images. Specifically, the pixel locations of common flow features (e.g., intensity fluctuations in the floor or sidewall boundary layers, rays of the laser sheet intersection with shocks, vortex cores, etc.) observed in both camera channels were noted from random pairs (sig./ref. pairs) from random model positions and random bursts. These random elements were used to give an averaged outcome, which was a practical necessity due to the volume of data that had to be analyzed from these tests. Once a sufficient number of points was found (at least 200, roughly uniformly distributed throughout the image plane), a function was fit to these data that maps the signal channel onto the reference channel. This function was a bivariate, 3rd-order polynomial of the form:

$$x_{px,ref} = c_{x,0} + \sum_{i=0}^{3} c_{x,3,i} x_{px,sig}^{3-i} y_{px,sig}^{i} + \sum_{i=0}^{2} c_{x,2,i} x_{px,sig}^{2-i} y_{px,sig}^{i} + \sum_{i=0}^{1} c_{x,1,i} x_{px,sig}^{1-i} y_{px,sig}^{i} \quad (3.1)$$

$$y_{px,ref} = c_{y,0} + \sum_{i=0}^{3} c_{y,3,i} x_{px,sig}^{3-i} y_{px,sig}^{i} + \sum_{i=0}^{2} c_{y,2,i} x_{px,sig}^{2-i} y_{px,sig}^{i} + \sum_{i=0}^{1} c_{y,1,i} x_{px,sig}^{1-i} y_{px,sig}^{i} \quad (3.2)$$

Once the coefficients in Eqs. 3 are fit, the transform was applied to all images in the signal channel, and the remapped images were saved before the remainder of the data analysis was commenced. A comparison between the unmapped (raw) images and remapped images can be found in Figs. 6a-d.

B. Camera Calibration

The camera calibration and subsequent image correction were used to quantitatively measure intrinsic and extrinsic imaging parameters, map image coordinates into the physical domain, and ultimately correct perspective and radial distortion in the images. Prior tests with valid calibrations used the method of Tsai successfully. [12] These tests necessitated a new method for calibrating the camera system. This new method utilized a ray-tracing-based simulation of the camera system to directly map pixel locations to locations in physical space. The simulation used a pinhole imaging approximation to model the optics along with a radial optical distortion model equivalent to that used in the Tsai method. Ultimately 11 parameters were optimized in these simulations including the lens focal length, the distance from the lens to the imaging plane (laser sheet), the x-, y-, and z-position at which the optical axis intersects the laser sheet, the azimuthal, polar, and roll angles of the camera system, and the first radial distortion coefficient. Additionally, two additional parameters were fit outside of the simulations, the horizontal and vertical shifts in the pixel location due to the image not being centered on the sensor. Table 2 summarizes the different camera calibration parameters, while Fig. 7 depicts the layout of the calibration environment including the relevant angles and distances.

To fit these coefficient parameters to the image data, a combination of image information and CAD models of the model/tunnel were used. First, for each data run, a mean image was constructed from all the positions and bursts of data. In this mean image, the pixel locations of any identifiable features associated with the tunnel and model were noted. Possible features included reflections off the model body and fins, the sting, the sidewalls, and the floor of the tunnel. These same locations were found in the CAD models of the particular run configuration, and their relative physical positions noted. The calibration parameters were fit in a ‘brute force’ manner; arrays of simulations were run in which a wide range of values (coarsely spaced) were selected for all parameters, and the physical locations implied by each simulation calculated. A series of different metrics for the simulation were calculated with respect to the measured positions in the CAD model, including the linearity and horizontalness of the laser scatter on the floor, the linearity and verticality of the model centerbody, and so forth. A minimum error was determined through these metrics, and the procedure repeated with a new range for all parameters around the previous minima. This procedure was repeated until the minimum was determined to with 0.1° or 1 cm depending on the type of unit. The observed RMS error following optimization was approximately 6 percent of the reference lengths.

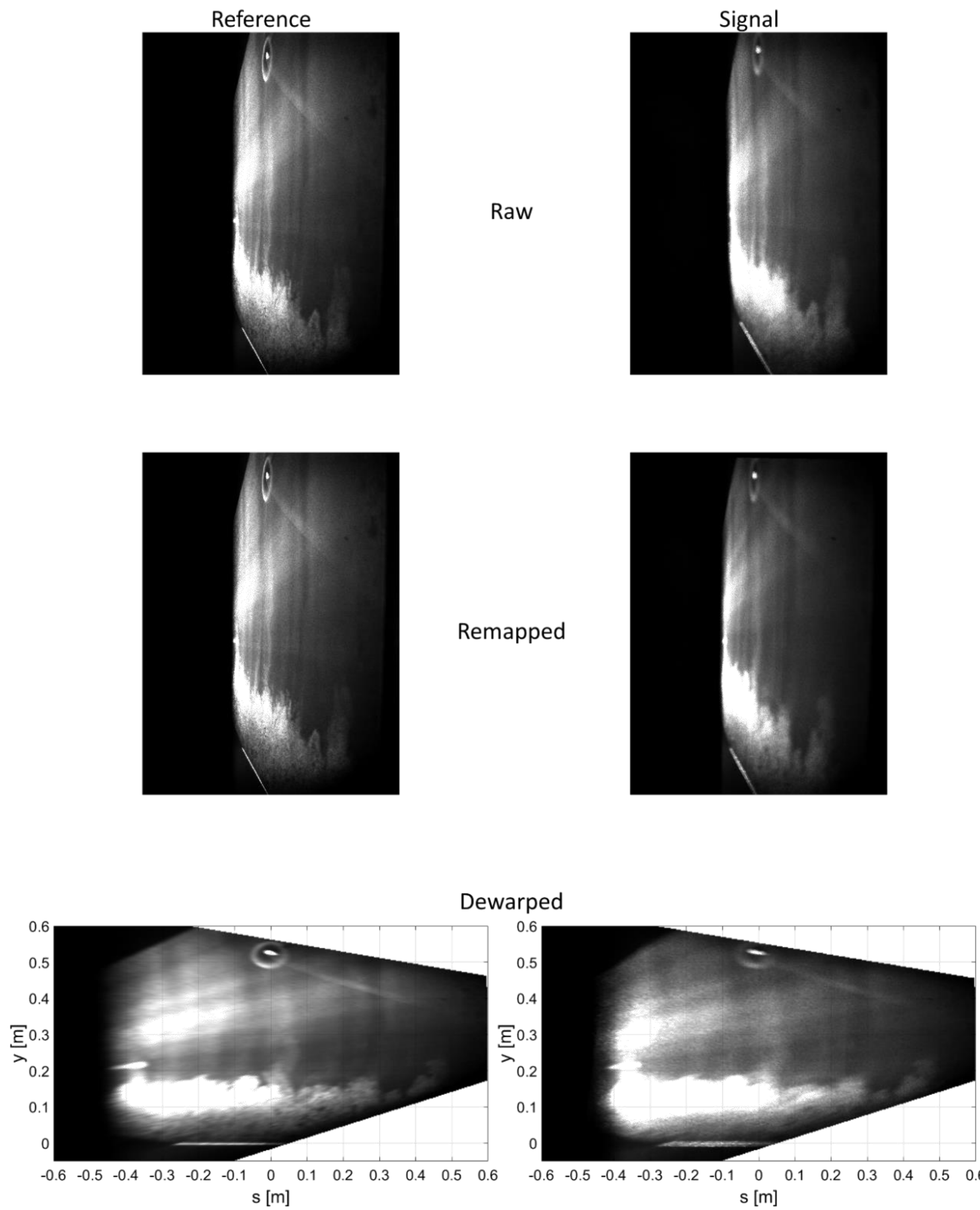

Figure 6. Stages of image preprocessing. Top row, raw images. Middle row, remapped images. Bottom row, fully dewarped and scaled images. The left column shows the reference data while the right column shows signal.

Table 2: Camera Calibration Parameters

Parameter	Description
θ_c	Centerline camera polar angle
ϕ_c	Centerline camera azimuthal angle
ψ_c	Camera roll angle
x_c	x-offset of camera optical axis from center of laser sheet
y_c	y-offset of camera optical axis from center of laser sheet
z_c	z-offset of camera optical axis from center of laser sheet
l_c	Distance from camera pinhole to laser sheet
f_c	Camera focal length, distance from pinhole to sensor
k_c	First radial distortion coefficient
os_x	Horizontal offset [px] of the image from the center of the sensor
os_y	Vertical offset [px] of the image from the center of the sensor

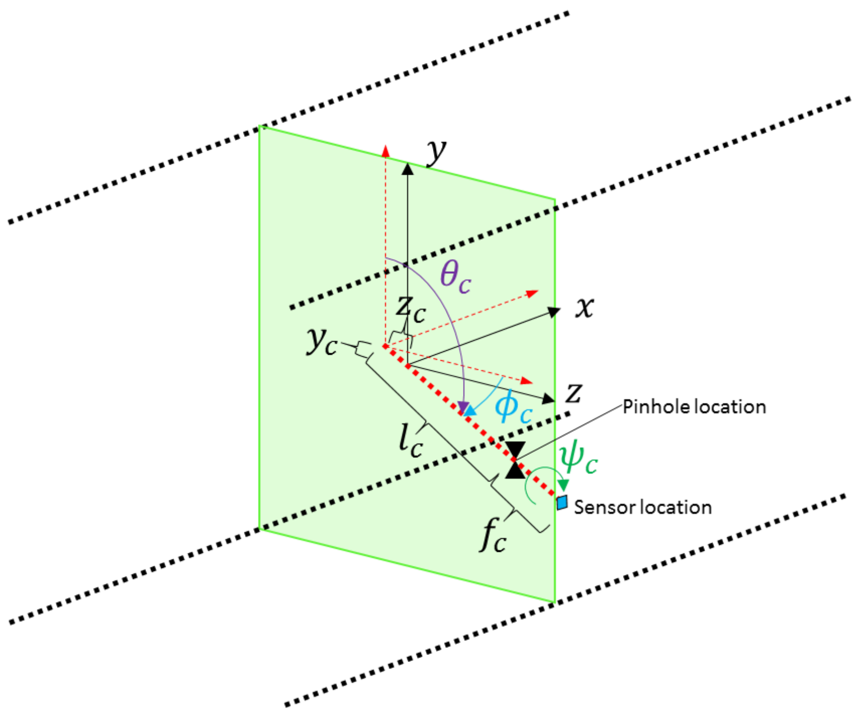

Figure 7. Diagram of calibration parameters.

C. Image Correction

The calibration parameters optimized during the camera calibration provide a pixel-wise mapping into physical space. However, the positions specified by the simulation method were nonuniformly spaced. To permanently correct the images, a new set of uniformly-spaced position data arrays were created with a user-specifiable spacing; the vertical and horizontal extents of these position arrays cover the same physical area as the camera simulation. While the selection of the spacing is largely arbitrary (does not affect the spatial resolution), the spacing was selected such that the vertical direction contained 256 pts. (256 pts. × 471 pts.). This selection was made as a balance between the grid resolution and processing time, with fewer points yielding a solution too coarse, and more causing the processing time to become excessive. Once these arrays have been created, the images are mapped onto this new uniform grid through Delaunay triangulation/interpolation. All images for both the reference and signal channels were processed in this way before the next steps of processing. Note that a Gaussian blurring filter (1.5-px stencil size) was applied to the images in the reference channel prior to this final step. This filter was used to match the blurring seen in the signal channel, improving the spatial overlap. Figures 6e and 6f show fully dewarped images along with their raw and initially remapped counterparts. The blurring filter has not been applied to the references images shown in Fig. 6.

D. LFM analysis

Sample data traces from the laser frequency monitor and the etalon can be found in Fig. 8 (subplots a) and b), respectively). The intensity data from the two channels of the laser frequency monitor were first scaled to overcome any mismatch between the two channels. Typically, the scaling factor imposed less than a 10-percent correction. The ratio of these two channels was taken (signal to reference) to acquire the transmission as a function of time. After first dividing the etalon trace by the LFM reference channel, each peak in the etalon data was detected and fit with a second-order polynomial to refine the center position. These positions (typically 10-11 peaks per scan) were then checked to ensure that the spacing between peaks was even. If so, a linearized frequency array was constructed through a least-squares fitting routine. These data were then used to map the reference absorption spectrum into the frequency domain. During these tests, the camera and laser were run at different frequencies (25 kHz and 100 kHz, respectively). To correctly down-sample the LFM trace, the 'Exposure Out' channel of the camera was monitored during testing; this channel nominally gives a 5V signal when the exposure is occurring and 0 V when inactive. When the exposure out was high, the point that fell within this region was selected as the correct point. It was discovered in later assessments of the data that the camera was not behaving as described during operation, instead outputting a quasi-sinusoid that never zeroed or hit 5V. A separate check was put in place to ensure that the time between selected data points was consistent and correct. If not, an alternative method was employed that detected the first valid point on the LFM trace then selected every fourth point moving forward. It is unknown what fraction of the data had this invalid behavior, but the correction method described was able to counteract it.

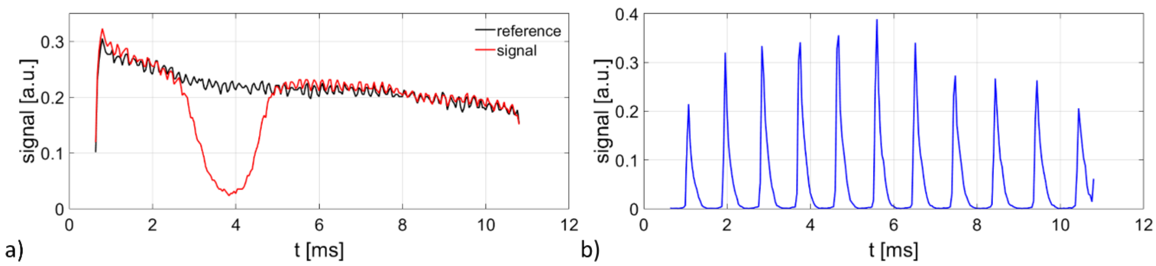

Figure 8. Diagnostic signal traces. a) LFM traces (reference and signal) and b) etalon trace.

E. Combining Data Sources

Although the camera exposures were synchronized during these tests, and the laser frequency monitor and cameras were triggered from the same source, the synchronization between these two data sources was not actively controlled. Moreover, the coarser frequency scans used during these tests in comparison to previous tests means that errors associated with the misalignment of these different sources would amount to a larger error than previous tests. For these reasons, particular focus was given to ensure that these data sources were properly aligned before the final Doppler shift evaluation.

1. Matching camera channels

The cameras were synchronized in a primary-secondary configuration during these tests, but the potential errors induced by misalignment of the data warranted checking the overlap between channels. For both the signal and reference channels, a time-trace of the signal intensity was constructed by summing the signal over a consistent, small region in each image; both traces were then normalized to peak intensity. In order to detect potential desync and correct it, one trace was first cropped by a certain number of points (between 0 and 5) at the beginning, and the other trace held constant, at which point the Pearson correlation coefficient was calculated between the two. This procedure was repeated for all values. Note that only the points up to and excluding the absorption feature (in the signal channel) were included. After this process was completed, the procedure was reversed, with the opposite trace being cropped and the other held constant, and the remainder of the procedure being the same. This procedure effectively allowed the correlation coefficient to be calculated for overlaps ranging from -5 to +5 images. The peak of the correlation function was then found and assumed to represent the correct temporal overlap between the two camera channels. No misalignments were detected during this assessment.

2. Overlapping LFM and camera

A similar procedure was used align the LFM and camera signals, this time comparing the two reference channels (camera and LFM reference channels). A one-dimensional array of intensity versus time was constructed from the set of images in the same fashion described above, and both this trace and the one from the LFM were normalized to peak intensity. Due to the differences in sensitivity and dynamic range of the photodiodes and the camera, the number of data samples per burst were often different between these two sources. In order to detect the correct overlap, the trace derived from the images (typically longer than that from the LFM) was cropped to the same number of points, and the Pearson correlation coefficient was calculated. This procedure was repeated, varying how many points at the beginning and end were cropped for a total range of -10 to +10 intervals. When complete, the correlation coefficient as a function of overlap position was mapped, and the peak of this function was assumed to be the correct overlap position. Figure 9 shows a sample of these correlation maps. This method (and the one described for just the camera channels) works because the sinusoidal oscillations on top of the burst profile (caused by the beat frequency of the acousto-optic modulators used in the laser) should be aligned between all data sources. The correlation coefficient shows a peak value when these peaks and troughs are well-positioned with respect to each other, and is much more sensitive and faster than visual verification.

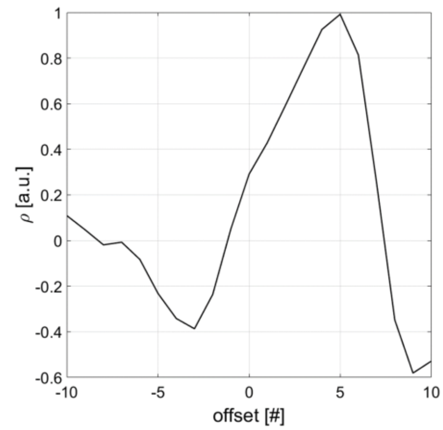

Figure 9. Pearson correlation coefficient showing overlap between camera and LFM signals, indicating the correct shift between the two to be 5 images.

An additional complication that arose during these tests was the dramatic mismatch in time traces for the LFM reference channel and the reference channel of the camera for some bursts. This mismatch occurred because of the beam alignment telescope and the more dramatic beam steering issues encountered during these tests. When the beam moved too far off the primary optical axis, the iris at the focus of the telescope would attenuate the beam's intensity, which was not seen on the LFM since it was sampled before the telescope. Figure 10 shows a comparison between an LFM trace and an integrated trace from the camera system (same burst); the feature in question is the different behavior between 0.5 and 3 ms (the grossly different slopes causes a stronger negative correlation than the positive correlation seen between the small oscillations). About one quarter of bursts suffered from this issue, though it did not affect the evaluation of Doppler shifts since the reference and signal camera channels both had this feature ingrained. This feature mismatch caused a poor correlation between the two reference sources for the purposes of the alignment described in this section. To counteract this issue, a modification to the above procedure was used when detected. A shorter trace was used (approximately 1/5 of the overall trace, and the peaks of the intensity oscillations were fit and divided by with a polynomial (intensity vs. time). This process removes the overall shape variation and improves the correlation approach previously described. Once the correct overlap had been determined, the image sets and LFM data were correctly cropped and saved into a combined data set for the next step of analysis. As a final note to this section of the data analysis, preventing this problem in the future requires the acquisition of more channels of data than were possible in these experiments. Specifically, to completely keep track of the data from pulse to pulse, the exposure-positive and record-positive traces from both cameras would need to be acquired in addition to both LFM traces and that of the etalon. During these tests, only 4 channels of data acquisition were available through the oscilloscope, which were reserved for absolutely essential data.

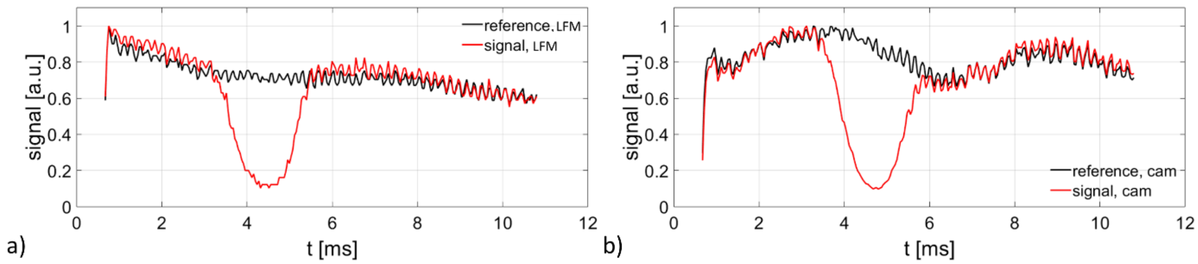

Figure 10. Comparison of LFM and camera traces when beam is severely out of alignment. a) LFM traces and b) integrated camera traces from the same burst.

F. Doppler Shift Evaluation

After the combination of data sources, the Doppler shift evaluation was carried out. In pixel-wise manner, an absorption spectrum was constructed from the time-series of images. This spectrum was then compared to the reference absorption spectrum from the LFM via cross-correlation. The spectra were first smoothed with a 5-point averaging filter. Next, both spectra were inverted such that the regions of unity transmission were zero and complete absorption was one. Zeros were used to pad the spectra, the number depending on the length of the original arrays. Finally, the mean of the beginning and end of each absorption trace was subtracted from their respective traces to prevent mean-biasing by noise during cross-correlation. Cross-correlation was then performed twice: once between the reference and camera spectra and once between the reference spectrum and itself (autocorrelation). The peaks of these functions were fit with an even-ordered polynomial (up to fourth-order, all odd-ordered terms omitted to prevent asymmetries) to refine the center position. The difference between the autocorrelation and cross-correlation peaks was then defined to be the frequency shift. This procedure was repeated for each pixel in the image. *A priori* rejection criteria were used to filter out evidently bad data including a filter for low signal (more than 5-percent of the points below the image noise floor), a saturation filter (more than 10-percent of points above 4025 counts), and a not-a-number (NaN) filter (more than 1-percent of the points registering as NaN, indicating something wrong with the previous steps of analysis). The amount of data removed via these filters varies significantly from burst to burst and scan to scan. For example, in these experiments image intensity saturation was the primary cause of pixel removal. Scans that contain many saturated pixels may have 10-20 percent of pixels removed in this manner. Other scans that don't suffer from this issue may not have any pixels removed. Typically, more pixels were removed from the West side of the tunnel, where the laser sheet was more focused and reflection from the windows and walls contaminated the images.

G. Correlation of Sums

The data taken in these tests had several obstacles that made it difficult to analyze compared to previous tests. The shallow camera and laser angles, the coarser frequency spacing, the beam steering issues encountered, and the spatial calibration issues described previously made the accuracy and precision of the Doppler-shift measurement far more critical than in previous tests. Furthermore, the data itself was noisier and had more signal conditioning issues than seen in previous applications of PB-CC-DGV, such as intensity skew and the variable intensity attenuation seen in the camera traces described in Section V.E.2. Two additional steps were applied to the data to improve the overall signal conditioning and make the Doppler shift calculation more robust. The first of these steps was 'correlation of sums.' Correlation of sums (COS) replaced ensemble averaging in this data analysis. In standard ensemble averaging, the mean Doppler shift of all available samples are averaged after calculation. Using correlation of sums, the actual absorption spectra for each pixel (and from the LFM) are averaged *before* the cross-correlation is performed. To achieve this properly, the frequency scaling and relative frequency of each burst must first match. The first burst of data for each measurement position was used as the reference; the frequency spacing was determined for the reference (LFM) absorption spectrum. Next, the reference spectrum from each subsequent burst for that model position were interpolated onto a common frequency axis. Finally, cross-correlation is performed between the reference LFM trace and the new interpolated spectrum; this process measures the relative spectral distance between the reference spectrum and the current burst of data. All of these shifts and rescaling coefficients are noted.

The next stage of this analysis was the averaging of the absorption spectra from the image data. On a pixel-wise basis, the spectrum from each burst of data was shifted according to the previously-calculated amount and interpolated onto a common frequency axis. After this all spectra from all bursts were summed and averaged (10 bursts model position, excluding data points in the same way as with single-burst analysis). At this point, a common, averaged reference spectrum and Doppler-shifted spectra were available. These data could then be analyzed according to the method described in Section V.F, or the data could be transferred onto the next stage described for further pre-conditioning of the signal.

The main advantage to correlation of sums is that it helps to suppress random errors found in the data (see Appendix I.D.2). By applying correlation of sums, the effective level of noise (both random and patterned) and random skew are diminished rapidly, leading to a more precise measurement. Since the calculation is done before the cross-correlation takes place, pixels that would otherwise be rejected due to poor correlation quality are often preserved, and more data are ultimately retained. However, the data are still susceptible to bias errors, and due to the small number of samples collected, is not free of the uncertainties caused by the random error sources.

H. Synthetic Spectrum

The final (optional) phase of signal conditioning is being called 'synthetic spectrum.' Synthetic spectrum (SS) fits a theoretical profile of the absorption well where the measurement is occurring (around 18789.3 cm^{-1}), which was calculated using the Forkey model for I_2 absorption.[13] However, the fitting procedure allows the amplitude and frequency scaling of the theoretical profile to vary so that the fit to the data is optimized, rather than focusing on adherence to the theoretical form. A comparison of raw, COS, and SS absorption spectra can be seen in Fig. 11. Procedurally, the data calculated through correlation of sums is used as the starting point. The reference spectrum and the spectrum at each pixel is then fit with a theoretical spectrum. The data is then passed onto normal evaluation (see Section V.F) using these synthetic spectra instead of the raw or pre-conditioned data.

The main advantage (as shown in Appendix I.D.3) of using the SS method is to eliminate common bias errors encountered when intensity skew is present in the data. The SS method is not effective at improving experimental noise, and thus does not improve measurement precision notably when used on individual bursts of data. Since the SS method uses a least-squares fitting procedure to carry out the operation, it is often susceptible to noise as much as the initial cross-correlation and polynomial fitting procedures that are used in those procedures. Consequently, even though experimental noise is removed from one calculation, it is present in the other, and no improvement is noted. However, when the data have already been noise-suppressed through the COS method, SS is highly effective at removing bias errors in the data caused by intensity skew, which is present in most of the data. It is through the combination of these two methods that the greatest overall improvement on the data was observed.

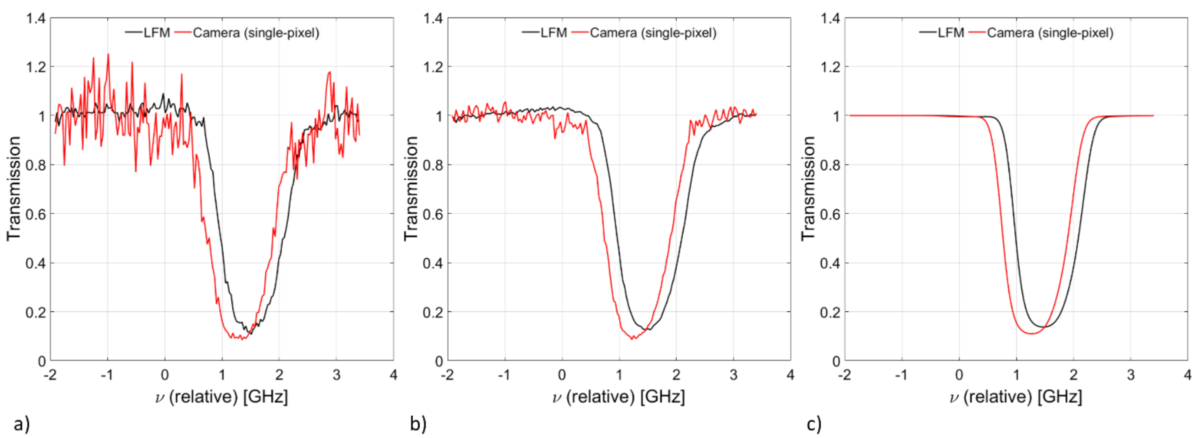

Figure 11. Comparison between absorption spectra using a) normal evaluation, b) correlation of sums, and c) correlation of sums + synthetic spectrum.

I. Velocity Evaluation

1. Measurement of $\hat{o}$-vector

The measurement of the observation vector and its spatial variation was determined using the camera calibration data. The ray-tracing simulation at its core provides an immediate measurement of the non-normalized x-, y-, and z-components of the observation vector. These components are then normalized such that observation vector has unit length. For later computations, these vector components are then interpolated onto the solution grid and rechecked to ensure unit length. Equation 4 defines the different components of the observation vector with respect to the local spherical coordinate system shown in Fig. 1b.

$$\hat{o} = (o_x, o_y, o_z) \tag{4.1}$$

$$o_x = \sin\theta_{\hat{o}} \sin\phi_{\hat{o}} \tag{4.2}$$

$$o_y = \cos\theta_{\hat{o}} \tag{4.3}$$

$$o_z = \sin\theta_{\hat{o}} \cos\phi_{\hat{o}} \tag{4.4}$$

2. *Measurement of $\hat{\imath}$-vector*

The laser propagation vector is determined through a combination of *in situ* measurements of the laser angle along with measurements made on the imaging data. The pointwise determination of the i-vector requires the measurement of two angles with respect to the tunnel coordinate system, the azimuthal angle and the polar angle. The azimuthal angle ($\phi_{\hat{\imath}}$) is taken from physical measurements taken in the tunnel of the laser sheet propagation direction. For all bursts of data, $\phi_{\hat{\imath}}$ was measured to be 2.24°. The polar angle ($\theta_{\hat{\imath}}$) was measured by measuring the direction of striations in the laser sheet on images that had already undergone dewarping. To do this, 7-10 lines corresponding to striations were selected manually in the images, and this procedure was repeated several times throughout a burst and across several bursts. This selection process resulted in a coarse, averaged measurement of the polar angle at those locations. A fitting procedure was then used which fit a sector of a circle (center position and distance) to the observed angular variations. This procedure smoothed the data and made the variation physically consistent (monotonically varying throughout the measurement region). The polar and azimuthal angles were then interpolated onto the measurement grid. Finally, the components of the i-vector were evaluated at the measurement locations by the following equations:

$$\hat{\imath} = (i_x, i_y, i_z) \tag{5.1}$$

$$i_x = \sin\theta_{\hat{\imath}} \sin\phi_{\hat{\imath}} \tag{5.2}$$

$$i_y = \cos\theta_{\hat{\imath}} \tag{5.3}$$

$$i_z = \sin\theta_{\hat{\imath}} \cos\phi_{\hat{\imath}} \tag{5.4}$$

Equations 5.1-4 are the standard components of the vector used in a spherical coordinate system (Fig. 1b) and thus require no further normalization.

3. *Velocity calculation*

As mentioned previously, the experimental configuration allowed the measurement to be considered one-dimensional over large portion of the measurement region. While manifestly untrue in some regions, the assumptions can be used as an estimate of the local streamwise velocity. The streamwise velocity can be calculated according to Eq. 2. When using this formulation, the $\hat{o}$ and $\hat{\imath}$ vector components are taken from the calculations explained in Sections V.I..1-2, the Doppler shift $\Delta\nu$ is taken from the Doppler shift calculation described in Section V.F-H, and the wavelength λ is assumed to be centerline wavelength of 532.217 nm.

VI. Results

A complete run of data is presented in Figure 12 including the average scalar field (average of 150 images and 10 bursts, for 1500 images total), streamwise velocity, and the velocity uncertainty. In these data, the CobraMRV model is at a 55° AoA, and the tunnel is running at a Mach number of 3.5 and unit Reynolds number of 9.9×10^6 1/m, corresponding to Case 5 in Table 1. Presented uncertainties generally range from 50 to 150 m/s (2σ, 95-percent confidence interval). For a detailed explanation of how uncertainties are calculated, refer to Appendix I. Note that the uncertainties presented in this section do not include the effects of biases caused by background artifacts (which are within the overall uncertainties) or (in the case of the velocity uncertainty) the presence of non-streamwise velocities. What is observed in Fig. 12 is the evolution of the CobraMRV flowfield as the model is translated to further upstream locations. Initially, the model is located downstream of the laser sheet. As the model is translated upstream, the bow shock becomes visible (x_m = 48-47 in.). The visible section of the bow shock appears to approach the boundary layer with further upstream translation (x_m = 46-41 in.). The foot of the separation shock associated with the SWTBLI becomes visible at x_m = 41 in., and the ensuing separation bubble grows before intersecting with the bow shock around x_m = 38 in. The downstream leg of this lambda shock structure falls rapidly within the center of the tunnel between x_m = 37-36 in., while remaining relatively substantial off the tunnel centerline. A region of expansion and accompanying reacceleration is then observed in the remaining model positions.

The noted flow structures can be better understood by performing a pseudotomographic reconstruction of this dataset. Figure 13 shows vectors resampled along the reconstructed centerline of this flowfield; the bow shock and lambda shock structures have been highlighted in red. The vectors indicate the presence of two small recirculation regions present within the separation bubble. It is possible that these structures are incipient or mobile rather than being multifocal, but the time-averaged nature of the data precludes further assessment. It will suffice in this case to indicate that such structures are present. Note that in the wake region, where the scattering signals were minimal due to low seed concentration, the velocity measurements are not available.

The other data sets collected during these studies allow for a check of basic fluid dynamic behaviors with the velocity measurements. One such assessment is the effect of Mach number on the bow shock structure; an assessment of effect of Mach number on these data are shown in Fig. 14. Here, reconstructed centerline velocity fields for three cases (1,4, and 7) taken at the same unit Reynolds number, AoA and fin angle are shown, with the only variable being the freestream Mach number (2.4, 3.5, and 4.6, Figs. 14a,b, and c, respectively). This comparison shows that the bow shock becomes progressively more swept back as the Mach number is increased. Additionally, the standoff distance, or more specifically the distance from the shock to the CobraMRV body, decreases with increasing Mach number. Both of these observations are consistent with the general understanding of compressible flow behavior. Figure 14d shows a direct comparison between the positions of the bow and lambda shock structures for the 3 Mach numbers. An interesting observation in this comparison is the effect on the lambda shock structure. Notably the size, shape, and position of the shock foot varies significantly with the Mach number variation. The most consequential reason for these changes is the variation of boundary layer thickness with Mach number, increasing from around 0.1 m at Mach 2.4 to 0.15 m at Mach 4.6 based on probe data.[2] This change alone accounts for the variation in streamwise position and height of the lambda shock structure, since it changes the point at which the bow shock encounters the boundary layer.

Another fluid dynamic effect which can be examined is that of Reynolds number on the character of the lambda shock structure. Figure 15 examines the observable changes in the lambda shock structure with Reynolds number variation; centerline velocity fields taken at Mach 3.5, AoA of 55°, and fin angles of 0° are presented at 3 different unit Reynolds numbers (3.3×10^6 1/m, 9.9×10^6 1/m, and 14.8×10^6 1/m, corresponding to cases 4, 5, and 6). The lambda shock structure shifts downstream from approximately x = 1.05 m to 1.1 m from lowest to highest Reynolds number. Moreover, the separation bubble becomes thinner (vertically) as the Reynolds number increases. Although not visible from this centerline presentation, a change in the three-dimensional character of the SWTBLI is also present, with the trailing edge of the lambda shock growing narrower with increasing Re. Other subtle changes are also present, such as the slope of the separation shock and the downstream edge of the lambda shock. Regardless of the Reynolds number, there is at least one region of separated flow present within each of these flowfields. While there isn't a significant variation in the boundary layer thickness at different Re, increasing the Reynolds number leads to more energetic (higher momentum) fluid within the outer regions of the boundary layer. This change in behavior results in the flow exhibiting inviscid flow characteristics deeper into the boundary layer. Similar behaviors were noted by Baldwin et al. when examining the Reynolds number dependence of swept STWBLI, noting that cases measured with higher Reynolds number exhibited a greater resistance to flow separation and a exhibited a downstream shift and reduction in overall expanse of the SWTBLI.[14] Ultimately, the ability to resolve these changes is indicative that the measurement techniques are capable of capturing the physical behaviors present in these flowfields. As a final commentary on Figures 12 through 15, a region of high velocity is observed immediately following the bow shock above y = 0.1 m to approximately y = 0.25 m, both along the centerline and part of the spanwise extent of the FOV. While the expected behavior is a decrease in velocity in this region due to the presence of the shock, the flow appears to accelerate. This region exists due to the changing measurement geometry in in these regions. With the flow (likely) at a slight downward angle following the shock, a positive velocity bias is imparted to the measurement due the local orientation of the sensitivity vector, which is equally sensitive to the vertical and streamwise components of velocity in this area (see Appendix I, Eq. A1 and Figs. A1 and A2 and the surrounding discussion for more details). These obvious physical inconsistencies are among the reasons it was recommended in Section III (and Section VIII to follow) for simulations to make direct comparisons with the Doppler shift rather than with the inferred streamwise velocity; doing so eliminates potential biases imparted by the streamwise assumption.

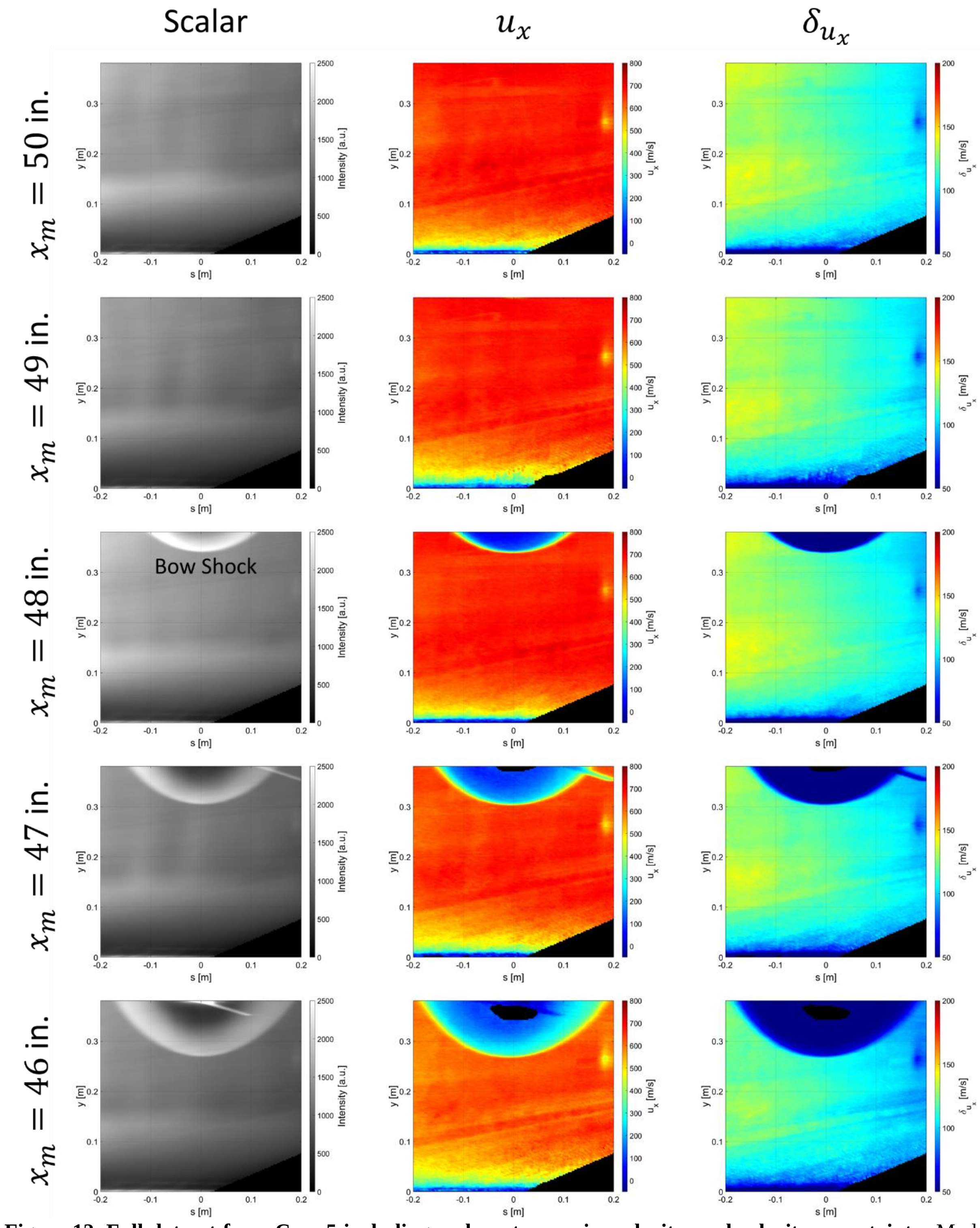

Figure 12. Full dataset from Case 5 including scalar, streamwise velocity, and velocity uncertainty. Model positions detailed in figure.

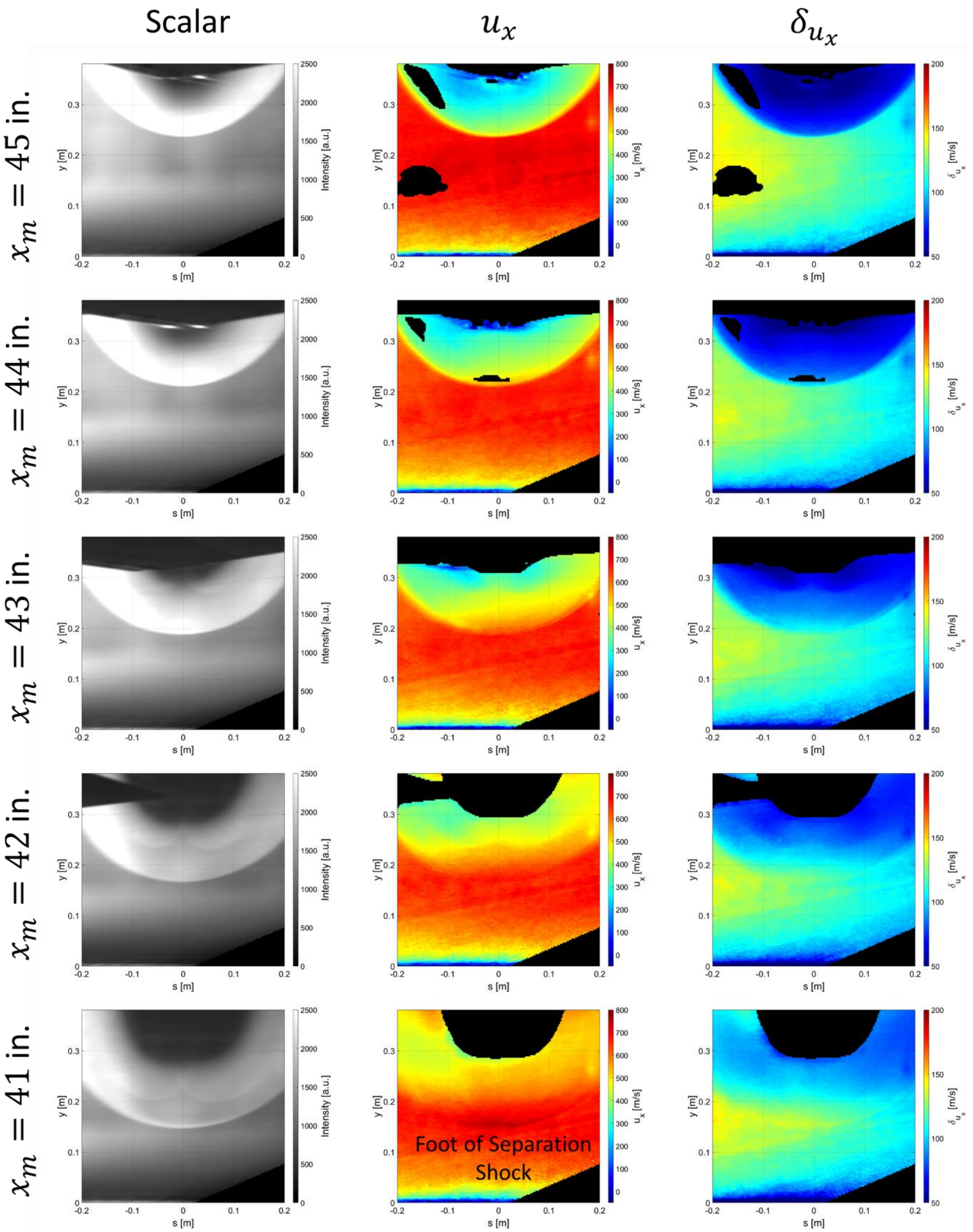

Figure 12. Continued.

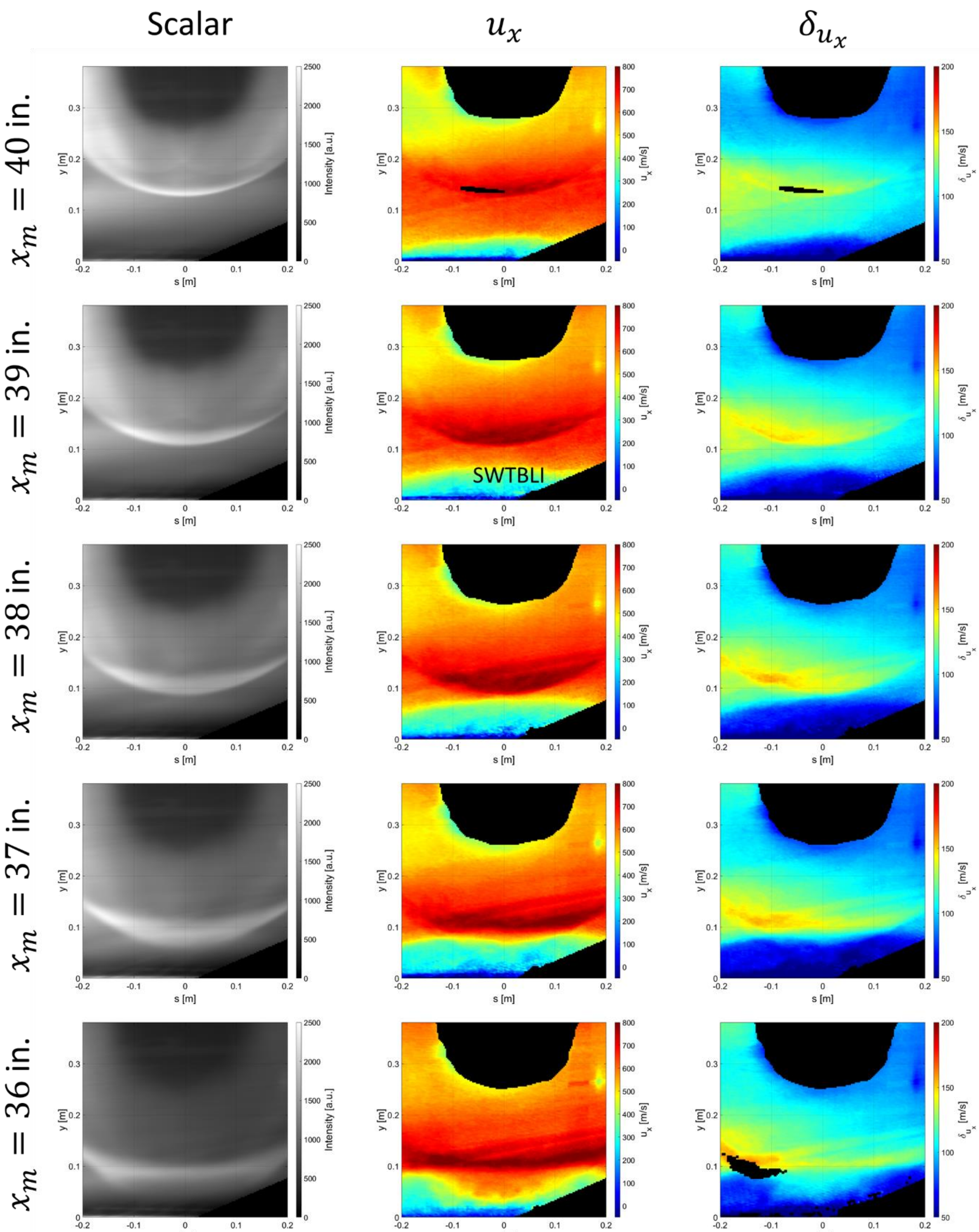

Figure 12. Continued.

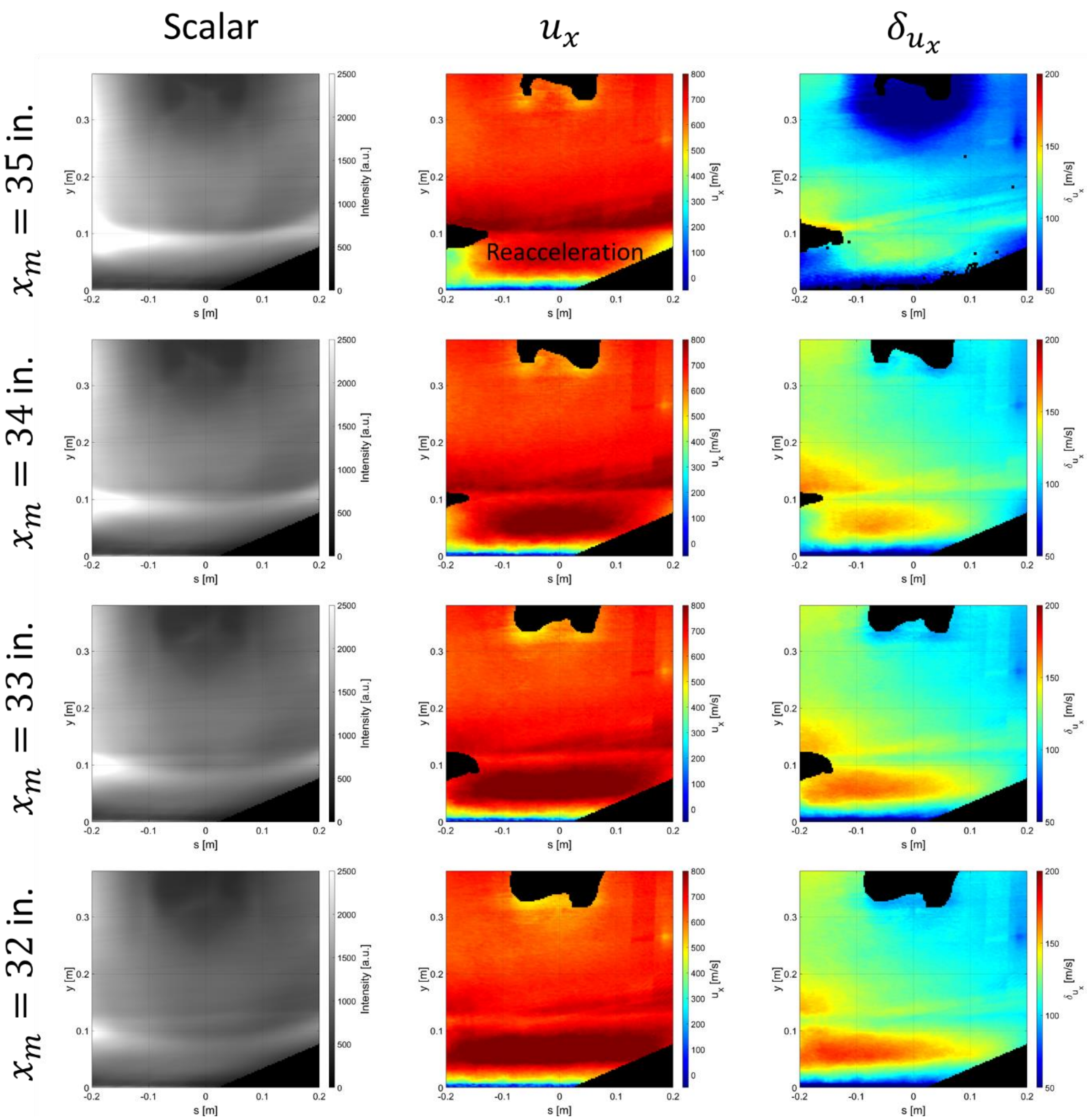

Figure 12. Continued.

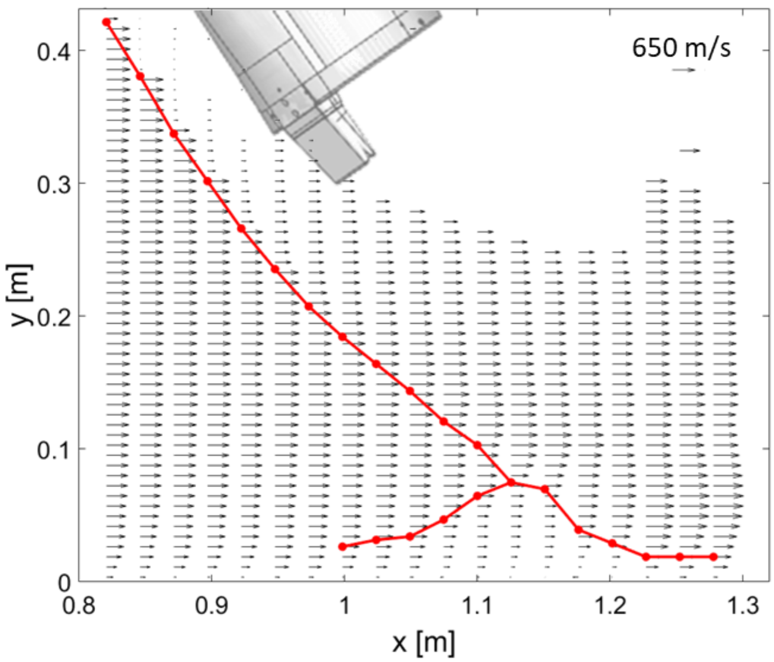

Figure 13. Reconstructed centerline streamwise velocity profiles/vectors for Case 5.

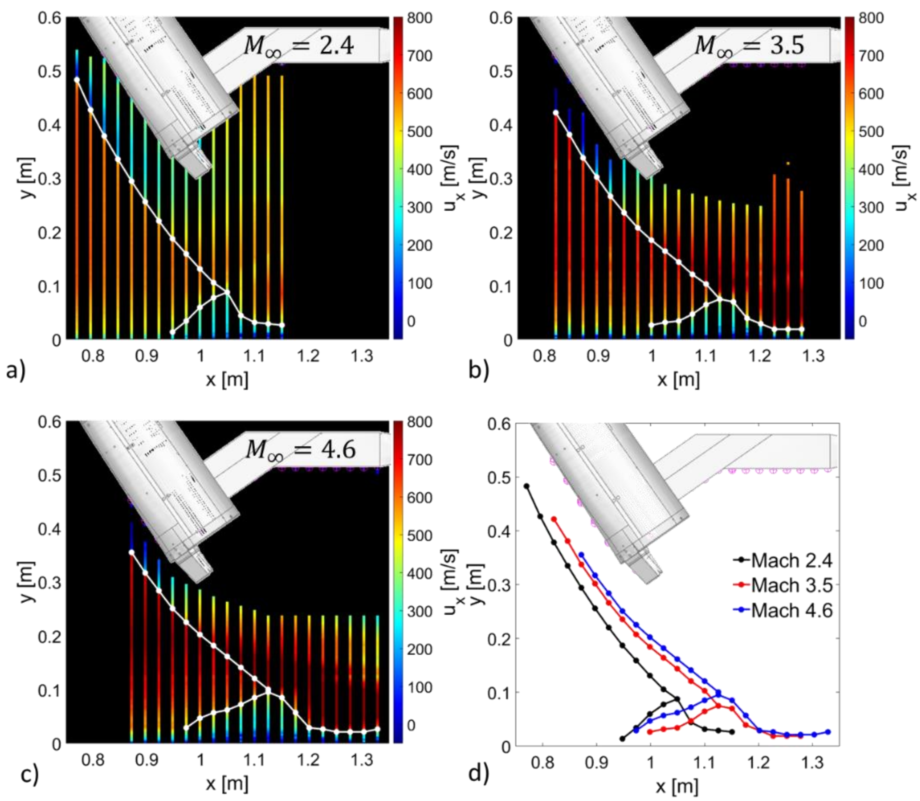

Figure 14. Comparison of centerline velocity fields as at different Mach numbers. a) Mach 2.4, b) Mach 3.5, and c) Mach 4.6. All cases Re = 9.9e6 1/m, AoA = 55°, F/A = 0°/0°. Data not available at all streamwise positions for all cases.

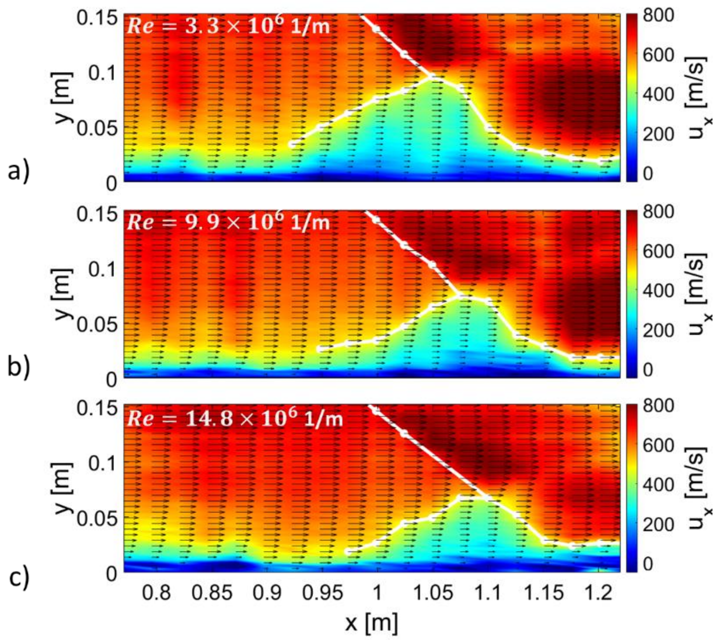

Figure 15. Effect of Reynolds number on CL SWTBLI. a) Re 3.3×10^6 1/m, b) 9.9×10^6 1/m, and c) 14.8×10^6 1/m. All cases M = 3.5, AoA = 55°, and F/A = 0°/0°.

VII. Measurement Assessment

A. Measurement Accuracy

A comprehensive assessment of the measurement accuracy and precision is difficult to perform in this experiment due to the practical nature of the flow; no universal standard exists for comparison. Therein lies the importance of the stated measurement uncertainties presented in Section VI and explained in Appendix I. However, a limited assessment of the measurement accuracy can be made with respect to the freestream velocity for the most downstream model positions. For this assessment, the model was sufficiently far downstream at some point in each run to enable an unperturbed view of the freestream. Figure 16 shows the mean freestream velocity extracted from each such position for all cases compared to the expected freestream velocity based on the tunnel conditions and isentropic flow relations; the mean and minimum uncertainty present within the freestream region are also plotted for each sample. There is some notable scatter in these data, and most cases show a positive bias with respect to the reference velocity determined from facility wall pressures. In all cases, the measured velocities are accurate to the expected values within their uncertainties (95-percent confidence interval), be it mean or minimum. The mean error was 5.2-percent and the RMS error was 5.4-percent of the expected values for all samples. In comparison to previous implementations of this technique, which showed errors around 1-percent, [8] the present measurements show a decline in accuracy. Unlike the previous experiments, which were largely optimized for the velocimetry, these experiments were intended to optimize the FOV for flow visualization purposes (see Section III and the discussion in Section VIII). Consequently, certain parameters selected for the experimental setup resulted in a deleterious increase in sensitivity. For a full discussion of these effects, see Section VIII and Appendix I.D.3.

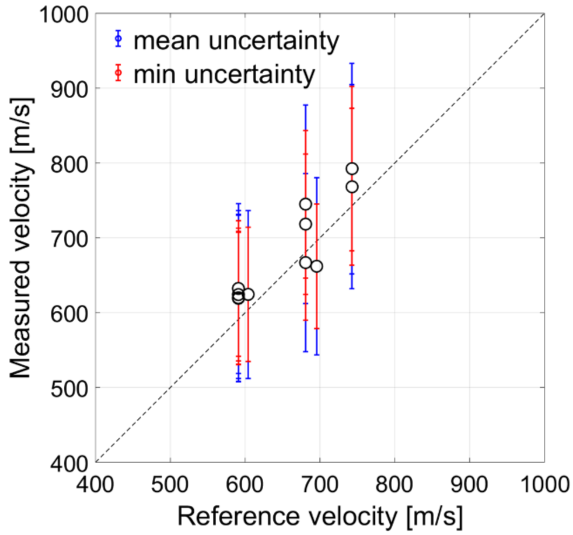

Figure 16. Accuracy of freestream velocity measurements.

B. Spatial Resolution

Spatial resolution can have different meanings depending on the type of measurement being made. In the case of these measurements, the definition of spatial resolution being used is the minimum possible length scale of a feature than can be resolved with the measurement system. While knowledge of the spatial resolution is crucial to any measurement, it is of particular concern in these measurements due to the imaging configuration. When viewing the laser sheet at grazing angles, there is a large differential between the magnification in different parts of the sheet, particularly in the sheetwise direction (**s**) in these tests. Figures 17a and b show the mean spacing between adjacent pixels within the measurement region. Notably, in the sheetwise direction (Fig. 17a), the spacing varies from fewer than 4 mm to over 10 mm. In contrast, the wall-normal direction sees a variation between 0.9 and 1.4 mm/px within the region of interest. These spacings represent the maximum (best) spatial resolution possible for these measurements. However, there are further complicating factors in these tests. Notably, the combination of the I_2 cell and relay imaging system caused the signal channel of the camera system to blur and have a slight double-image. The adverse effects on the spatial resolution can be assessed (in part) by using the image of the dotcard calibration target. In summary, it is a two-part procedure. Firstly, the amount of blur in the image is computationally assessed using the dots on the calibration target as a reference. Secondly, the effect that blurring has on the contrast of the image is assessed at the experimental resolution. Specifically, the spatial resolution is considered to be the minimum wavelength for which there is still 4-percent contrast. The combination of these two steps allows the spatial resolution of the measurement in the vertical and horizontal directions to be assessed at each calibration point. The spatial resolution is then interpolated on to the solution grid. The results of this assessment are shown in Figs. 17c-d. The spatial resolution in the sheetwise direction is found to range between 13 and 21 mm, exhibiting a marked gradient similar to the sheetwise pixel spacing though less exaggerated. In the wall-normal direction, the spatial resolution is found to range from 2 to 6 mm.

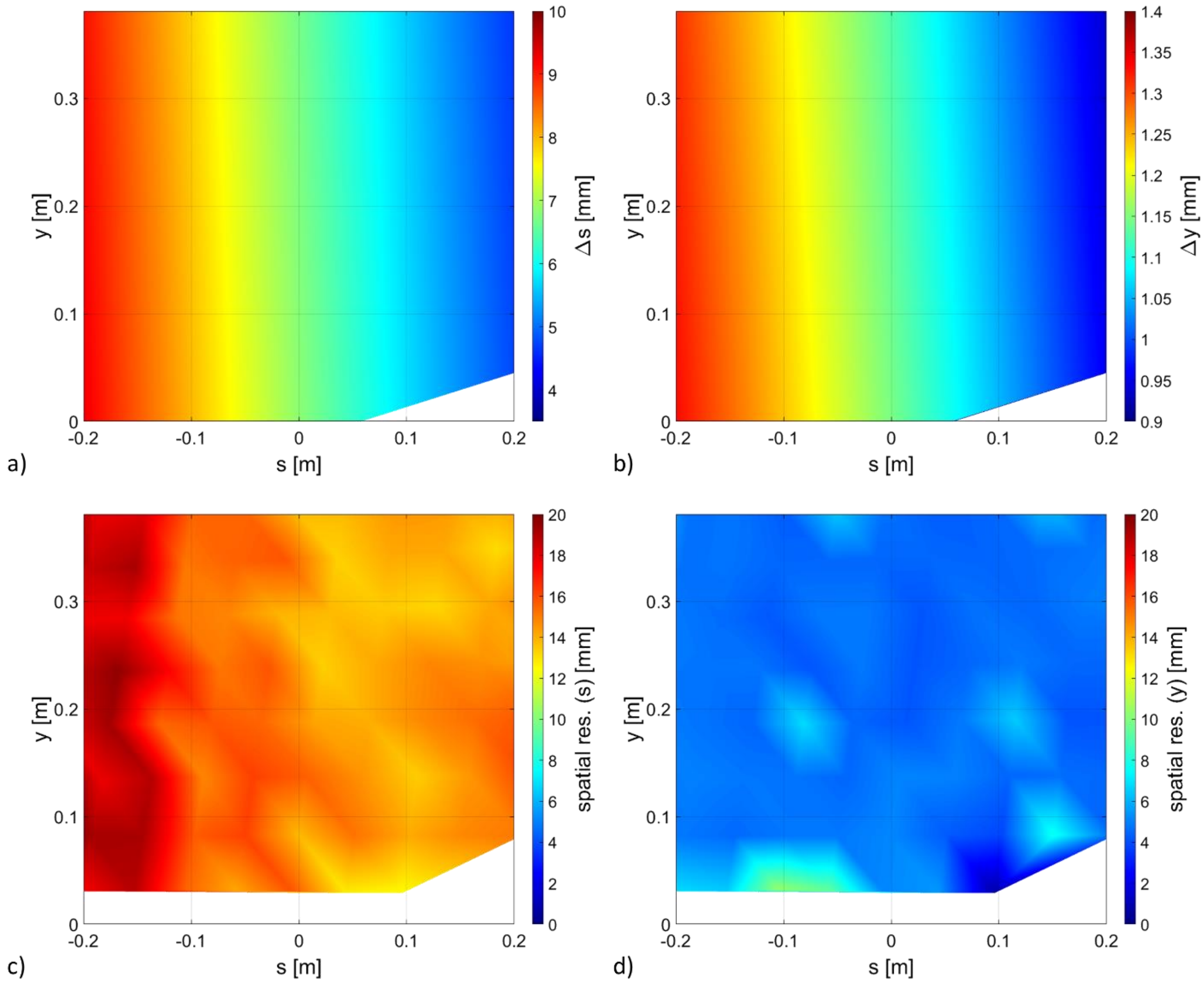

Figure 17. Spatial resolution. a) sheetwise pixel spacing, b) wall-normal pixel spacing, c) sheetwise spatial resolution (4-percent contrast), and d) wall-normal spatial resolution (4-percent contrast).

VIII. Discussion

The preceding description and assessment of the CobraMRV velocimetry experiments reveal certain limitations to the quality of the measurements imposed by the initial design of the experiment. It should first be noted that the experiment was designed to emphasize the flow visualization as it had the highest chance for success. The laser sheet was supposed be as orthogonal to the flow as possible, and the camera was positioned to view as much of the span of the tunnel as it could. This arrangement approximately aligned the sensitivity vector of the measurement to the streamwise direction of the tunnel – resulting in measurement of arguably the most important velocity component. In these capacities, the experiments were successful. However, these decisions about the orientation of laser and camera also led to an array of problems that affected most elements of the PB-CC-DGV analysis.

The decision to use glancing angles for the camera and laser sheet is the main contributing factor to the difficulties experienced in camera calibration. In a typical experiment, the camera's optical axis is often situated orthogonal to the laser sheet. If the laser sheet or camera are misaligned in those circumstances by a degree or two, the effect on the measurement is minimal, resulting in a slight measurement and magnification errors. However, by situating the camera and laser as was done in this experiment, the measurements became much more sensitive to small deviations in laser sheet angle. A deviation of a single degree in the laser sheet constitutes a very large deviation (on the order of 10s of cm) in *perceived* location. This increased sensitivity, the instability in the laser pointing direction, and the very long beam path all contributed to the challenges encountered with the camera calibration. These issues with the camera calibration led to a cascade of difficulties through the entire data analysis process. However, the camera calibration was not the sole problem created by this decision. Another major issue was the contributions made to the measurement uncertainty. The decision to use glancing angles have a two-fold effect on these elements. First, the x-component of the sensitivity vector is quite small in magnitude (only 0.15 at the center of the FOV out of a maximum possible sensitivity of 2.0). Second, the uncertainties with respect to the azimuthal angles are increased. For this reason, nearly 80 percent of the measurement uncertainty (in velocity, Fig. [21] in Appendix I) is the result of uncertainties in the angles. It is likely that a factor of two or more improvement could be seen in the measurement uncertainties if more consideration were given to the selected angles. Finally, the large gradient in measurement spacing (see Fig. 17) was the direct result of the decision to orient the laser and camera as was done in these experiments. Effectively, the way the experiment was set up made the velocity measurement as sensitive as possible to the quantities that are the most difficult to control or measure.

Another detrimental decision was to utilize a large FOV. Again, while apt for flow visualization, this decision complicated the experiments markedly. The large FOV required a short focal length lens to be placed very close to one of the windows – essentially necessitating the DRIS used in this experiment. If a FOV even half the size was acceptable, it is likely that a more traditional imaging system could have been used. This change would lead to a great improvement to the spatial resolution of the measurements, and would likely reduce or eliminate the blurring seen in the signal channel of the camera system to levels observed in previous experiments (the blurring was the same, but the ultimate effect was larger because of how zoomed-out everything was), further improving the spatial resolution.

Despite the above statements, it is important to remember that the measurements fulfilled their purpose. Nonetheless, reflecting on these limitations can help to improve future studies, especially if the velocimetry is the primary goal of the measurement. The main improvements to these measurements would be:

- Increase the inclination of the laser sheet and camera
- Use a smaller field of view
- Utilize an additional camera calibration
- Reduce the laser scatter by routing the sheet out of a window on the east side of the tunnel
- Reduce the tunnel humidity during testing
- Condition and monitor the laser beam and sheet

The decision to set the laser sheet and cameras with opposing angles was a useful tool to isolate the streamwise velocity component and to increase the intensity of the light scattering, allowing lower laser-pulse energies to be used. These effects would not be hindered by further inclination of the laser and cameras. In fact, the x-component of the sensitivity vector would elongate in that circumstance, leading to less susceptibility to small angular changes, but also increasing the magnitude of the observed Doppler shifts, which would aid in the data analysis as well. Most of the other problems described previously also would be alleviated to some extent, depending on how significant the changes in angle were. From the perspective of measurement uncertainty, a balance between the different angular contributions would need to be struck. As an example of the improvements that would be achievable, a 15-20° azimuth for both camera and laser sheet would yield a 6- to 10-percent reduction in the angular contributions to uncertainty, while increasing the measured Doppler shifts by greater than 4 times. Thus, the overall measurement uncertainty would decrease dramatically by 50 to 75 percent, similar to the oblique shock experiments done previously.[8] Full implementation of all of the ideas set forth in this section would reduce the uncertainties further, possibly in excess of a 90-percent reduction. Realistically, the FOV in these tests could have been reduced by a factor of 2 while still capturing the entire region of interest near the tunnel centerline. Along with the other factors associated with the angular changes, the spatial resolution of the measurements would see a marked improvement as well, the extent of which would depend on all the above factors. Additionally, utilizing a smaller FOV may enable a higher camera repetition rate (e.g. 50 or 100 kHz), which would improve the flow visualization elements of the tests and the uncertainty associated with the Doppler shift measurements.

In addition to these two major changes to the measurement, smaller adjustments could be made that would improve different elements of this experiment and the overall results. One such change would be to perform an additional, independent camera calibration, such as the method of Zhang.[15]. Having an additional calibration that was independent of the measurement plane would allow the parameters evaluated in the original calibration to be verified, and would allow for calibration issues like the one described at the start of Section V to be readily detected and corrected if necessary. Another simple change would have been to route the laser sheet out of the tunnel on the East side rather than allowing it to hit one of the spars. This change would reduce the background scatter present in every data set and the associated measurement biases they impart. Reducing the tunnel humidity during testing would benefit the experiments notably, reducing the small (few-percent) deviations observed in the force and moment coefficients between dry and humid operation of the tunnel. The tunnel humidity was maintained at a relatively high value while collecting data to increase the seed density and thus improve the signals observed in the experiments. Reducing the humidity would require the use of more laser energy to make up for the loss in seed density. If done in conjunction with the reduction in background scatter described in the preceding point, sufficient signal could be attained at much lower humidity. Finally, various improvements could be made to the beam conditioning elements that were used in these tests. The pointing stability of the laser was a challenge to accommodate during analysis, and there are various means available to alleviate some of those difficulties. Improving the pointing stability would likely require the use of a beam imaging or relay system. In such a system, rather than utilizing a single stabilizing telescope as in the current setup, a series of telescopic imaging relays would be placed within the beam path. Doing so would allow the image of the beam at the frequency-doubling crystal within the laser to be relayed over to the measurement location. While such a setup would not completely eliminate beam wandering, the effects of the long beam-path would be reduced, and the overall amount of deflection caused by the pointing instability would be almost eliminated. However, such a system would be challenging to set up and maintain; frequent checks to the alignment and accuracy of the system would be required. Additionally, a surveillance system could be set up to monitor the beam position of the laser sheet burst-to-burst. Such a system would entail placing 2 or 3 additional cameras around the test section, which would trigger during a burst of the laser and capture an image of the mean laser sheet. With proper spatial calibration, the three-dimensional orientation of the sheet could be directly evaluated and compared to the manual measurements made in the current experiment. Alternative methods of achieving this sheet-monitoring system could be used as well, such as one- or two-camera photogrammetry. Finally, a procedural change that would aid in the calibration procedure would be to allow the laser to fire for an hour or more before checking the alignment with the alignment beam. With the combination of these different changes, a much more robust velocimetry experiment could be made.

Another point of discussion is regarding the validation of simulations with these data. While the measured velocities were nominally streamwise, as explained in Section III, the assumption which underlies that evaluation is known to be invalid in certain regions of the flowfield. While velocity is a more intuitive quantity to compare with simulations, it may make for a more robust comparison to instead compare directly with the measured Doppler shift. To achieve this, velocity components within the simulation could be combined with measurements made of the sensitivity vector components by Eq. 1.2. Using this procedure, which is operationally simple to conduct, would eliminate the innate bias resulting from the limitations in the model. It is unclear if the measurement uncertainties would be improved by this process; most of the uncertainties associated with the angles would have to propagate to the calculated Doppler shift. The main advantage would be to eliminate the assumption of having a principally streamwise sensitivity vector. Both of these options will be available for calculation.

IX. Conclusions

This paper summarized the application of the PB-CC-DGV technique to the flowfields around a CobraMRV scale model in the NASA Langley 4-foot Supersonic Unitary Plan Wind Tunnel. The focus of this analysis was a single experimental case, but the results can be generally applied to the other data sets as well. The experimental design, methods, data analysis, and measurement uncertainty were described in detail. Finally, a single, complete data set was presented. The flowfield presented involved a three-dimensional, shock-boundary layer interaction followed by a complex wave interaction further downstream. Assessment of the accuracy of freestream velocities indicated a varied bias in terms of magnitude and direction. A mean error of 5.2-percent of the reference velocities was observed for all cases. The assessment of overall measurement uncertainties found velocity uncertainties to lie between $\pm$50 and $\pm$150 m/s in general (95-percent confidence interval), with the mean value in the freestream about $\pm$120 m/s. The measurement uncertainty is dominated by angular uncertainties associated with the shallow angles at which the data were acquired, accounting for nearly 80 percent of the overall uncertainty. A series of recommended improvements were made, which detail methods for improving the velocimetry. Based on the current data, it is estimated that the angular uncertainties could be reduced by 6- to 10-percent, while the overall Doppler shift magnitude could be increased by greater than 4×, leading to an overall reduction in uncertainty of 50 to 75 percent. Full implementation of the ideas expressed in Section VIII would reduce the uncertainty further.

Appendix I. Measurement Uncertainty

The PB-CC-DGV technique is subject to uncertainties and errors associated with the measurement process and analysis of data. This section will expound the various sources of uncertainty prevalent during the CobraMRV tests. The following analyses expand on the analyses found in last year’s report.

A. Measurement Biases

While there are numerous biases in various component calculations that constitute the overall measurement, there are certain overarching issues that directly bias the final results. Notable among these are biasing by non-axial velocities and biasing by motion of the laser sheet. The full expression for the axial velocity can be expressed as:

$$u_x = \frac{\lambda \Delta \nu}{(\hat{o} - \hat{\imath})_x} - \frac{1}{(\hat{o} - \hat{\imath})_x} \left[(\hat{o} - \hat{\imath})_y u_y + (\hat{o} - \hat{\imath})_z u_z \right] \quad \text{(A1)}$$

The bias term in Eq. A1 (the terms following the – sign) are very difficult to quantify in these experiments due to the large spatial variation in velocity. One metric that can be considered is the ratio of different components of the sensitivity vector to the streamwise component. Figure A1 shows the 'axiality' of the measurement, while Fig. A2a-b show the relative magnitude of the wall-normal and spanwise components to the axial component, respectively. Note that axiality is defined as the ratio of the streamwise component of the sensitivity vector to the overall magnitude of the sensitivity vector at the same location; the closer to unity this quantity is, the more valid the assumption used in the u_x calculation is. As explained in Section III, the experiments were designed to minimize the influence of these different velocity components on the measurement. Figure A1 shows this to be true over approximately one quarter of the measurement area. However, many sections of the measurement region have a disproportional bias toward the other components, notably away from the center of the laser sheet. The divergence of the laser sheet was larger than that of the camera field of view, and consequently the components cease to cancel each other out as they do near the center of the laser sheet. In these regions the ratio of the sensitivity vector components may exceed a factor of 5 in some areas. For most of the flowfield, where the streamwise component of velocity is dominant, the contribution is likely small. Regions that possess larger transverse and spanwise velocity components will ultimately determine the magnitude of this bias. For example, the region near the windward (compressive) face of the CobraMRV will have a transverse velocity component nearly equal to the streamwise velocity due to geometric considerations. In these same regions, the respective components of the sensitivity vector are in favor of the transverse component by a factor of 2 or more. It would thus be a poor assumption to consider the Doppler shift to result mostly from the streamwise component, and comparisons should be made with respect to the Doppler shift instead to avoid this direct bias.

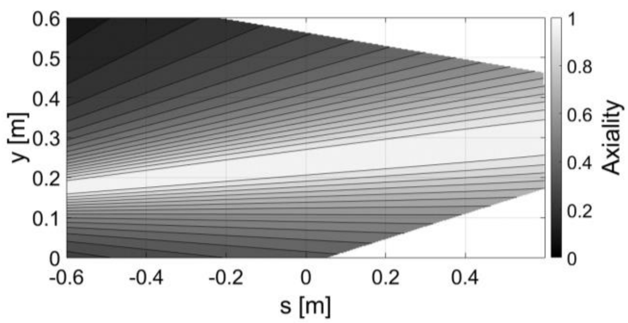

Figure A1. Spatial distribution of axiality of measurement sensitivity vector.

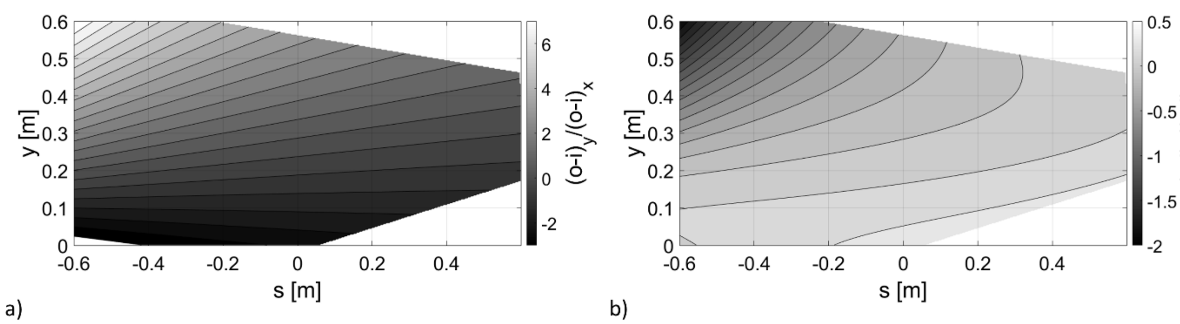

Figure A2. Relative magnitudes of wall-normal and spanwise components of sensitivity vector to the streamwise component. a) Wall-normal/streamwise and b) spanwise/streamwise. Note that the color range differs for each figure.

Another intrinsic bias to these measurements is the motion of the laser sheet. Throughout a burst, the pulse-burst laser has some issues maintaining pointing stability due to thermal lensing within the amplifiers. This effect is compounded by a long beam path and multiple passes through the tunnel sidewall boundary layers, which marginally affect the beam direction through changes in refractive index; the laser beam shifts around in both the transverse and streamwise directions during a measurement. As a consequence, the Doppler shift that is being measured with the technique is not a singular Doppler shift, but is an amalgamation of the different Doppler shifts seen at all different moments considered in the measurement. As the magnitude of this effect is a strong function of the local velocity components and the specifics of the motion, assessing the magnitude and direction of this bias is difficult. However, the bias would likely appear as a pseudorandom oscillation superimposed on the absorption spectra, and thus the effects are captured in Section AI.D to follow.

One prominent bias to the entire measurement process is the presence of background artifacts in the evaluated Doppler shift and everything that follows. A sample full Doppler-shift field is shown in Fig. A3; this field contains mostly freestream flow. The expected form of this field is a smooth, lateral gradient across the field of view due to the variation in observation angle. Instead, various artifacts appear in the background of the field. These artifacts exist for numerous reasons. Reflections of the laser beam off the tunnel spar cast light over most of the test section. The decision to position in the beam in this manner was made to eliminate the need for a laser barrier, and to keep the angle of the laser sheet as shallow as possible. This reflected light is seen by both channels of the camera system. Additionally, it is possible that some of the light scattered by the fog is reflected back toward the camera by any surface, though the contribution is likely small. The direct effect of the reflected light, regardless of source, is to impart a bias to the measured Doppler shift. In the context of these data, some fraction of the light at each pixel location is a combination of the desired light and the background reflections. If the background reflections are minute, the effect on the measurement is also. If not, the measurement can be biased (usually toward lower velocities) in two ways depending on the magnitude of the effect and the size of the Doppler shift. For small Doppler shifts, the effect is to broaden the absorption wells, leading to a bias toward zero in the case of background reflections. If the Doppler shifts are sufficiently large, a secondary absorption well may appear in the data, which could be used to disambiguate and remove the bias. Unfortunately, the former case is true in these data sets owing to the shallow laser and camera angles chosen. The prominent bias caused by the light reflected off the CobraMRV model is a prime example of this sort of bias. However, many of the artifacts observed in the data (from the spars, for example) are actually a bias toward a larger Doppler shift. While reflections of scattered light are possible, as noted above, a more likely explanation is something known as camera misalignment artifacts. Camera misalignment artifacts occur because the two cameras do not see *exactly* the same field of view at the same angles. While the camera calibration procedure (Section V.A-C) can correct alignment issues in the imaging plane, doing so does not affect the background of the images in the same way. The backgrounds will have slightly different physical scaling and alignments due to the difference in camera viewing direction. Similar effects can be seen if the calibration of the two images is not done properly, or the degree of focus in the reference and signal images do not match. Little can be done to correct these types of biases, but their magnitude can be estimated by observing the magnitude of their bias against the unbiased regions, where possible. What is observed in the average are differential Doppler shifts in the range of 15-20 MHz. Depending on their location within the field of view, this range of values may amount to between 25 and 100 m/s in the final velocity fields.

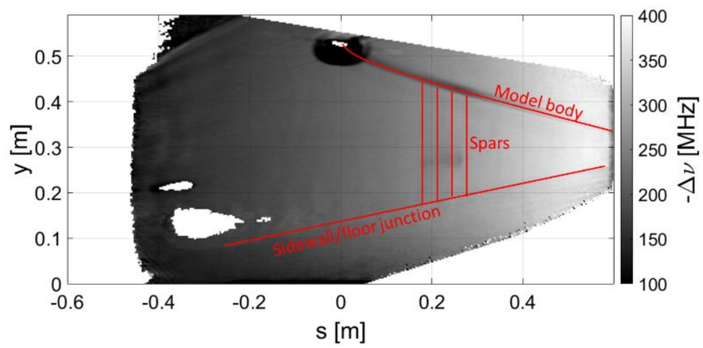

Figure A3. Sample Doppler shift field with background artifacts highlighted and identified.

B. Spatial Uncertainty

The uncertainty inherent in the spatial calibration process, as described in Section V.B, results in an uncertainty in the spatial positions. Specifically, the uncertainty in the selection of calibration points in the image and the limited number of calibration points and the accompanying lack of precision in the calibration procedure lead to an uncertainty in the calibration coefficients. In turn, these uncertainties limit how well the spatial positions are known. To understand the breadth of this uncertainty, a series of Monte Carlo simulations were carried out, in which the nominal values found during calibration were perturbed by random amounts commensurate with their uncertainties, and simulations were run in this manner until the sample standard deviation converged to within 0.1 μm. Table A1 lists the different calibration parameters and their associated uncertainties used in these studies. Note that the uncertainty values represent the 95-percent uncertainty threshold. Refer to Fig. 7 and Table 2 for a description of the different calibration parameters.

Table A1: Summary of Calibration Parameters and Associated Uncertainties

ϕ_o [°]	θ_o [°]	ψ_o [°]	y_c [m]	z_c [m]	f_c [m]	l_c [m]	os_x [px]	os_y [px]
-7.0 $\pm$ 0.5	86.0 $\pm$ 0.5	0.3 $\pm$ 0.2	-0.20 $\pm$ 0.02	0.00 $\pm$ 0.02	0.0352 $\pm$ 0.020	1.25 $\pm$ 0.05	-35 $\pm$ 2	0 $\pm$ 2

The associated uncertainties in the measured spatial positions are summarized in Figs. A4a and b, for the sheetwise and wall-normal directions, respectively. Within the region of interest, these uncertainties range from approximately 12.5 mm up through 25 mm in the sheetwise direction, and 5 mm through 10 mm in the wall-normal direction. These values represent the uncertainty in each location caused by the uncertainty in the camera calibration parameters. For example, at the location (s,y) = (-0.1 m,0.1 m), the positional uncertainties are found to be $(\delta s,\delta y)$ = ($\pm$0.017 m,$\pm$0.005 m). Thus, the sheetwise location lies between -0.083 m and -0.117 m, and the wall-normal position lies between 0.095 m and 0.105 m.

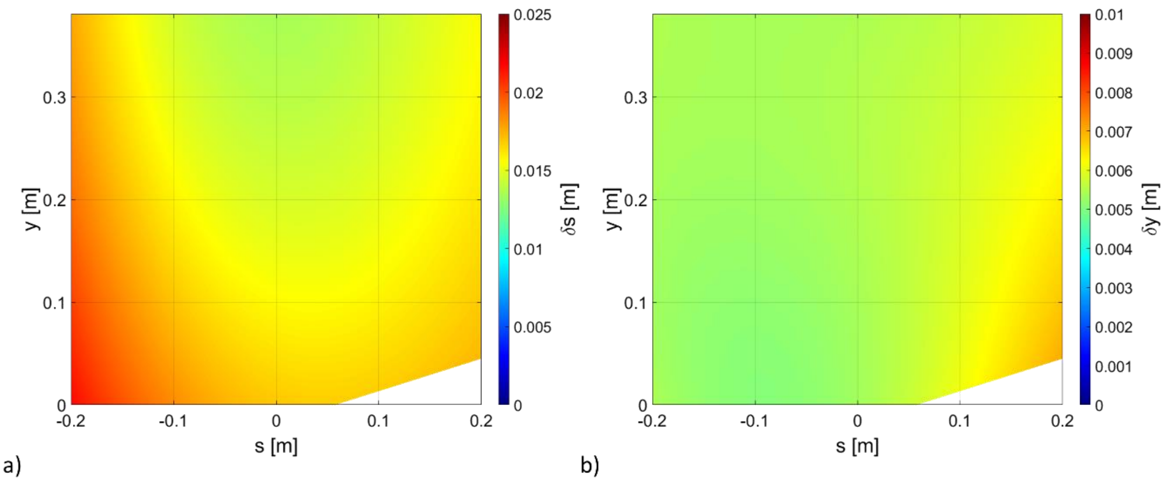

Figure A4. Positional uncertainties resulting from calibration uncertainties. a) Sheetwise uncertainty and b) wall-normal uncertainty.

C. Doppler-Shift Uncertainty

The overall uncertainty calculations will be presented along with the additional uncertainties associated with the use of the COS and SS methods. To summarize the previous results, and those applicable to single-burst Doppler-shift measurements: the measurement uncertainty is a function of the spectral resolution, the spectral skew, and the level of noise (both random and patterned) present in the absorption spectra. These different factors contribute nonlinearly to the measurement uncertainty.

1. *Single scan uncertainty*

The data in these tests exhibited approximately 2-percent noise levels in the reference (LFM) spectra and nearly 10-percent noise levels in the signal (camera) spectra as is evident in Fig. 10a. Spectral intensity skew was within the range -0.1 to 0.1. To assess the uncertainty, Monte Carlo simulations were carried out in which random values of these different parameters within the specified ranges were superimposed on synthetic absorption spectra with approximately the same spectral range as the measurements (overall range and frequency interval). Simulations were run until the measurement statistics converged to within 0.01 MHz; approximately 2×10^7 simulations were completed. The associated measurement uncertainty (95-percent confidence interval) for a single scan, plotted as a function of Doppler shift magnitude is shown in Fig. A5. A nearly constant uncertainty is observed of approximately 27.5 MHz (corresponding to 50 m/s in the center of the flow), indicating that the measurement algorithms are unbiased with respect to the magnitude of Doppler shift. This uncertainty is slightly less than a single bin (i.e., image or scan frequency increment), but is a substantial fraction of the typical Doppler shifts seen in these experiments (between -400 and -100 MHz).

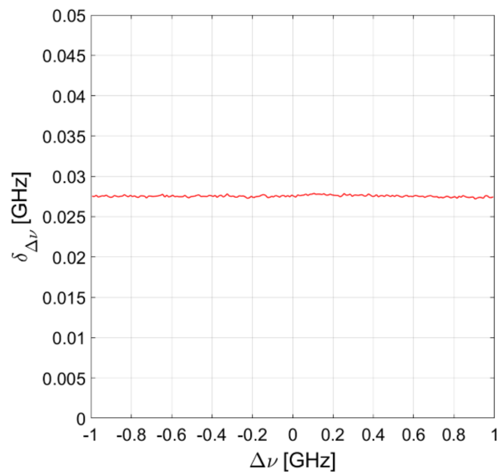

Figure A5. Uncertainty in measured Doppler shift (normal evaluation) as a function of Doppler shift magnitude and direction.

2. *Correlation of sums*

The correlation of sums method works to suppress random and semi-random sources of uncertainty such as noise and intensity skew (assuming its presentation random and not systemic). To evaluate the effects of the correlation of sums method on the measurement uncertainty, a set of Monte Carlo simulations were conducted. For a given initial noise level, varying numbers of samples (with a fixed Doppler shift) were averaged, and this procedure for the averaged spectra was repeated until the uncertainty statistics converged. Different noise levels were tested in this manner, and the results are presented in Fig. A6. The COS method has a strong suppressive effect on the Doppler-shift measurement uncertainty. Notably, the attenuation of the measurement uncertainty scales as approximately $1/\sqrt{n}$, where n is the number of samples used in the COS averaging. For the present data, where the number of samples in consideration ranges from 1 to 10, a greater than 3-fold improvement to the measurement uncertainty was possible through this method, though biases were likely still present in the data.

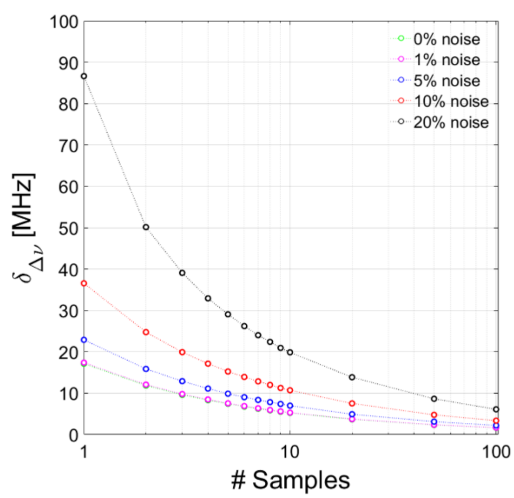

Figure A6. Measurement uncertainty of COS evaluation method as functions of the number of samples included in the calculation and the noise level of the spectra.

3. Synthetic spectrum

The synthetic spectrum method is specifically intended to suppress the effect of spectral intensity skew that has previously been found to both impose a bias on the data and to make measurements less precise. To evaluate the effect of the synthetic spectrum has on data, the same Monte Carlo method has been employed as explained in previous sections. In these simulations, the typical noise levels seen *after* COS processing has been used as the RMS noise levels, spectral skew in both the reference and signal spectra ranging from -0.25 to 0.25, and Doppler shifts ranging from -1 to 1 GHz. Simulations were conducted until convergence to 0.1 MHz in the standard deviation were achieved (approximately 1×10^{8} samples). During these simulations, both the standard and SS methods were conducted on each sample, and the deviations from the true value evaluated for both.

The results of these simulations are presented in Fig. A7; the observed errors are segregated by Doppler shift direction. The errors show that two primary extrema result from specific combinations of Doppler shift direction and reference and signal skew. While the errors observed near zero-skew are similar for both the standard and SS methods, the accuracy is improved as skew values are increased. A factor of 5 improvement is observed in these cases data when using the SS method. Restating for reference, the typical skew values observed in these data were around 0.1 in magnitude, which is an average improvement of a factor of 4 within the applicable range. These simulations suggest that the SS method provides an effective way of suppressing skew-induced bias errors without having to use arbitrary-order polynomials to make the corrections. Note that the measurement precision is not affected significantly by this method.

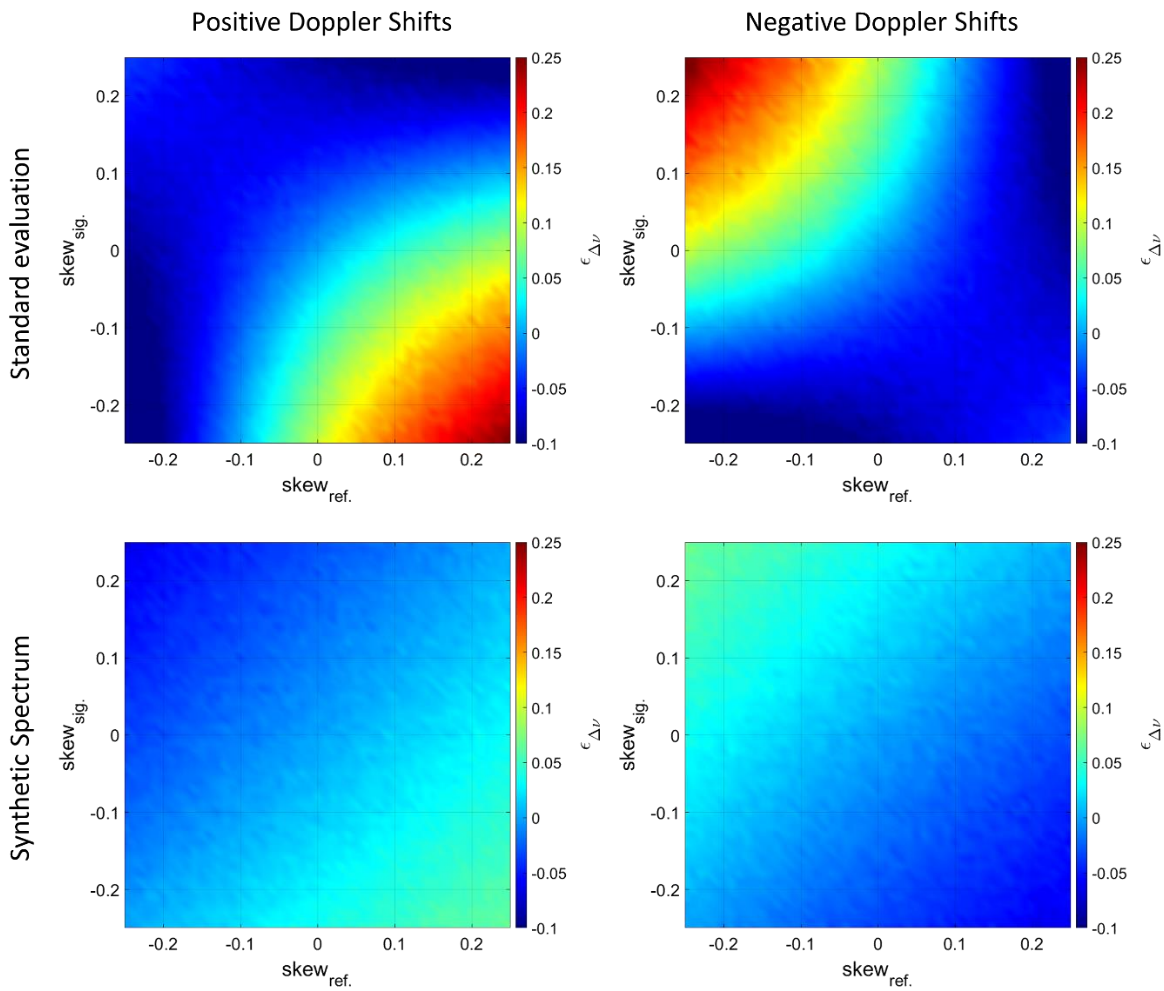

Figure A7. Fractional errors for standard and synthetic spectrum evaluation methods. Top row, standard evaluation. Bottom row, SS evaluation. Left column, positive Doppler shifts. Right column, negative Doppler shifts.

D. Velocity Uncertainty

Uncertainty in the streamwise velocities is a function of the uncertainty in the Doppler shift, uncertainty in the wavelength, and the uncertainty in the components of the sensitivity vector. The overall uncertainty in the streamwise velocity can be expressed as:

$$\delta u_x = \left[\left(\frac{\partial u_x}{\partial \lambda}\delta\lambda\right)^2 + \left(\frac{\partial u_x}{\partial \Delta\nu}\delta\Delta\nu\right)^2 + \left(\frac{\partial u_x}{\partial(\hat{o}-\hat{\imath})_x}\delta(\hat{o}-\hat{\imath})_x\right)^2\right]^{\frac{1}{2}} \tag{A2.1}$$

$$\frac{\partial u_x}{\partial \lambda} = \frac{\Delta\nu}{(\hat{o}-\hat{\imath})_x} \tag{A2.2}$$

$$\frac{\partial u_x}{\partial \Delta\nu} = \frac{\lambda}{(\hat{o}-\hat{\imath})_x} \tag{A2.3}$$

$$\frac{\partial u_x}{\partial(\hat{o}-\hat{\imath})_x} = -\frac{\lambda\Delta\nu}{(\hat{o}-\hat{\imath})_x^2} \tag{A2.4}$$

Equations A2.1-4 are derived from the definition of streamwise velocity (Eq. 2) processed with the standard (linear) uncertainty operator. The uncertainty in the Doppler shift has been described in the preceding sections, but the uncertainty in the wavelength and observation vectors will be discussed in this section.

1. *Uncertainty in wavelength*

The wavelength of the laser is both measured before the tests using a wavemeter and is independently verified by comparing the reference I_2 absorption spectrum to a theoretical model. Consequently, the uncertainty in this term is quite small, but non-zero. For simplicity, it is assumed that the uncertainty in the wavelength is the total spectral distance scanned during the measurement: $\delta\lambda = (\lambda_{end} - \lambda_{start})$. This quantity varies from measurement to measurement, but is approximately 0.00175 nm for the average scan range.

2. *Uncertainty in sensitivity vector*

The streamwise component of the sensitivity vector can be expressed as:

$$(\hat{o}-\hat{\imath})_x = \sin\theta_{\hat{o}}\sin\phi_{\hat{o}} - \sin\theta_{\hat{\imath}}\sin\phi_{\hat{\imath}} \tag{A3}$$

Equation A3 follows directly from the definitions of the $\hat{o}$ and $\hat{\imath}$ vectors in Eqs. 4 and 5, respectively. Evaluating the uncertainty in these data can be achieved using either standard uncertainty propagation or Monte Carlo simulations. The standard uncertainty propagation can be expressed as:

$$\delta(\hat{o}-\hat{\imath})_x = \left[\left(\frac{\partial(\hat{o}-\hat{\imath})_x}{\partial\theta_{\hat{o}}}\delta\theta_{\hat{o}}\right)^2 + \left(\frac{\partial(\hat{o}-\hat{\imath})_x}{\partial\phi_{\hat{o}}}\delta\phi_{\hat{o}}\right)^2 + \left(\frac{\partial(\hat{o}-\hat{\imath})_x}{\partial\theta_{\hat{\imath}}}\delta\theta_{\hat{\imath}}\right)^2 + \left(\frac{\partial(\hat{o}-\hat{\imath})_x}{\partial\phi_{\hat{\imath}}}\delta\phi_{\hat{\imath}}\right)^2\right]^{\frac{1}{2}} \tag{A4.1}$$

$$\frac{\partial(\hat{o}-\hat{\imath})_x}{\partial\theta_{\hat{o}}} = \cos\theta_{\hat{o}}\sin\phi_{\hat{o}} \tag{A4.2}$$

$$\frac{\partial(\hat{o}-\hat{\imath})_x}{\partial\phi_{\hat{o}}} = \sin\theta_{\hat{o}}\cos\phi_{\hat{o}} \tag{A4.3}$$

$$\frac{\partial(\hat{o}-\hat{\imath})_x}{\partial\theta_{\hat{\imath}}} = -\cos\theta_{\hat{\imath}}\sin\phi_{\hat{\imath}} \tag{A4.4}$$

$$\frac{\partial(\hat{o}-\hat{\imath})_x}{\partial\phi_{\hat{\imath}}} = -\sin\theta_{\hat{\imath}}\cos\phi_{\hat{\imath}} \tag{A4.5}$$

These have been expressed here to show the theoretical dependence on the different angles. Due to the significant spatial variations observed in these data sets, Monte Carlo simulations have been performed within the spatial calibration environment described in Section V.B to evaluate the propagation of these uncertainties. Figures A8a and b show the spatial distributions of the absolute uncertainty and fractional uncertainty, respectively. The absolute uncertainties indicate surprisingly little spatial variation (~5 percent max-min variation), the majority of this stemming from the streamwise instability in the laser sheet (ϕ_i). However, it is important to realize that the magnitude of the streamwise component of the sensitivity vector is itself small. Thus, as shown in Fig. A8b, the uncertainty is a substantial fraction of the local sensitivity vector, between 14 and 22 percent within the mapped field of view, so the magnitude of this uncertainty is significant. The values presented are all 95-percent confidence interval uncertainties.

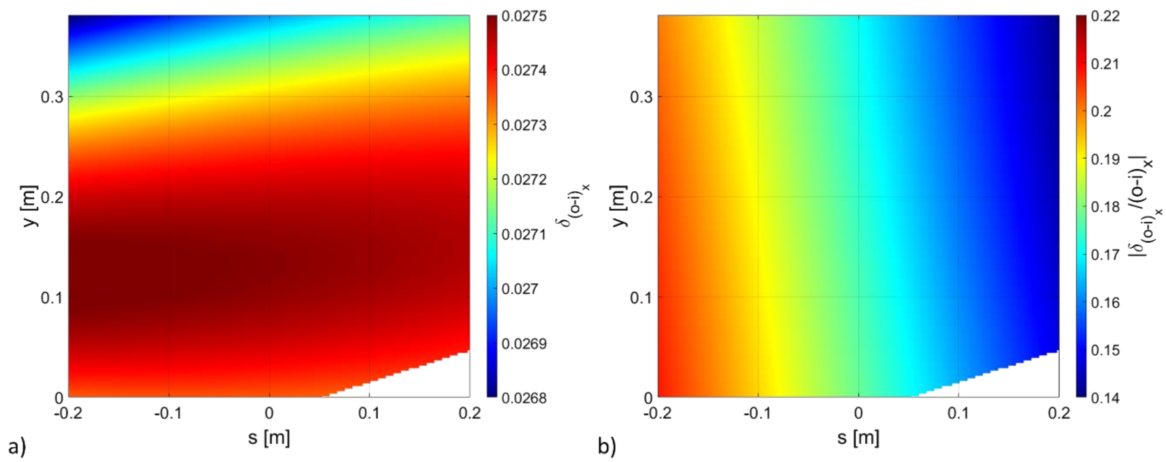

Figure A8. Uncertainty in $(\hat{\boldsymbol{o}} - \hat{\boldsymbol{\imath}})_x$ component of sensitivity vector. a) absolute uncertainty and b) fractional uncertainty.

3. Compiled uncertainty

With these component uncertainties estimated, the overall uncertainty in measured velocity can be assessed. Figure A9 shows several different uncertainty calculations based off of the different evaluation methods: standard, COS, and SS along with the associated velocity fields. The velocity field was taken from the tunnel freestream (x_m = 50 in.), wherein the boundary layer is the only significant gradient present. The velocity fields are similar in magnitude. The single-burst measurement in Fig. A9a still retains the spatial inhomogeneities associated with boundary layer structures, and the spatial precision is markedly worse than the COS or SS methods of evaluation. Likewise, the SS velocity field in Fig. A9e has an improved spatial precision over the COS method in Fig. A9c, and has also corrected some of the high-velocity biased regions around y = 0.175 m. The 95-percent confidence interval uncertainties reveal much about the relative effects of the different evaluation methods presented. The measurement uncertainty associated with standard evaluation show magnitudes ranging from roughly 50 to 200 m/s. A notable spanwise gradient is present, stemming from the spatial distribution of the sensitivity vector component across the region of interest. In comparison, the uncertainties for the COS and SS evaluation methods are markedly lower, ranging from 50 to 150 m/s typically; little difference is observed between the COS and SS methods, as expected from the preceding analysis (the primary effect being an improvement in accuracy, not precision). These figures obviate the improvements offered by these evaluation methods. Despite these improvements, the uncertainties constitute a substantial fraction of the freestream velocity, which is approximately 680 m/s under these test conditions. The minimum uncertainty is nearly 7 percent of this velocity with peak uncertainties in excess of 25 percent. Note that the biases imparted by the various background artifacts fall well within these uncertainty ranges as well, so further development of their influence is omitted. As with previous sections, all uncertainties stated are for a 95-percent confidence interval.

Figures A10a-c reveal the distribution of the overall uncertainty among the constituents for the three evaluation methods. As expected, errors associated with the laser wavelength are small. The standard Doppler shift evaluation (Fig. A10a) indicates the Doppler shift uncertainty accounts from nearly 45 percent of the overall uncertainty. The various components of the $(\hat{o} - \hat{\imath})_x$ uncertainty account for most of the remainder, notably the azimuthal angular components. Due to the experimental configuration, sensitivity to the polar angular components is quite small, since the polar angular components are near maxima. The COS and SS methods in Figs. A10b and c, respectively, indicate that nearly 80 percent of the uncertainty results from uncertainty in the sensitivity vector. It is important to remember that the absolute uncertainties present in the sensitivity vector are effectively constant, irrespective of how the Doppler shift is evaluated. These methods are able to suppress random uncertainties and particular biases that affect the Doppler shift measurement. The sensitivity vector is an average quantity as utilized in the analysis, and consequently any advantage achieved through use of an average is applied with each method by default. A discussion about improving the uncertainty is found in Section VIII.

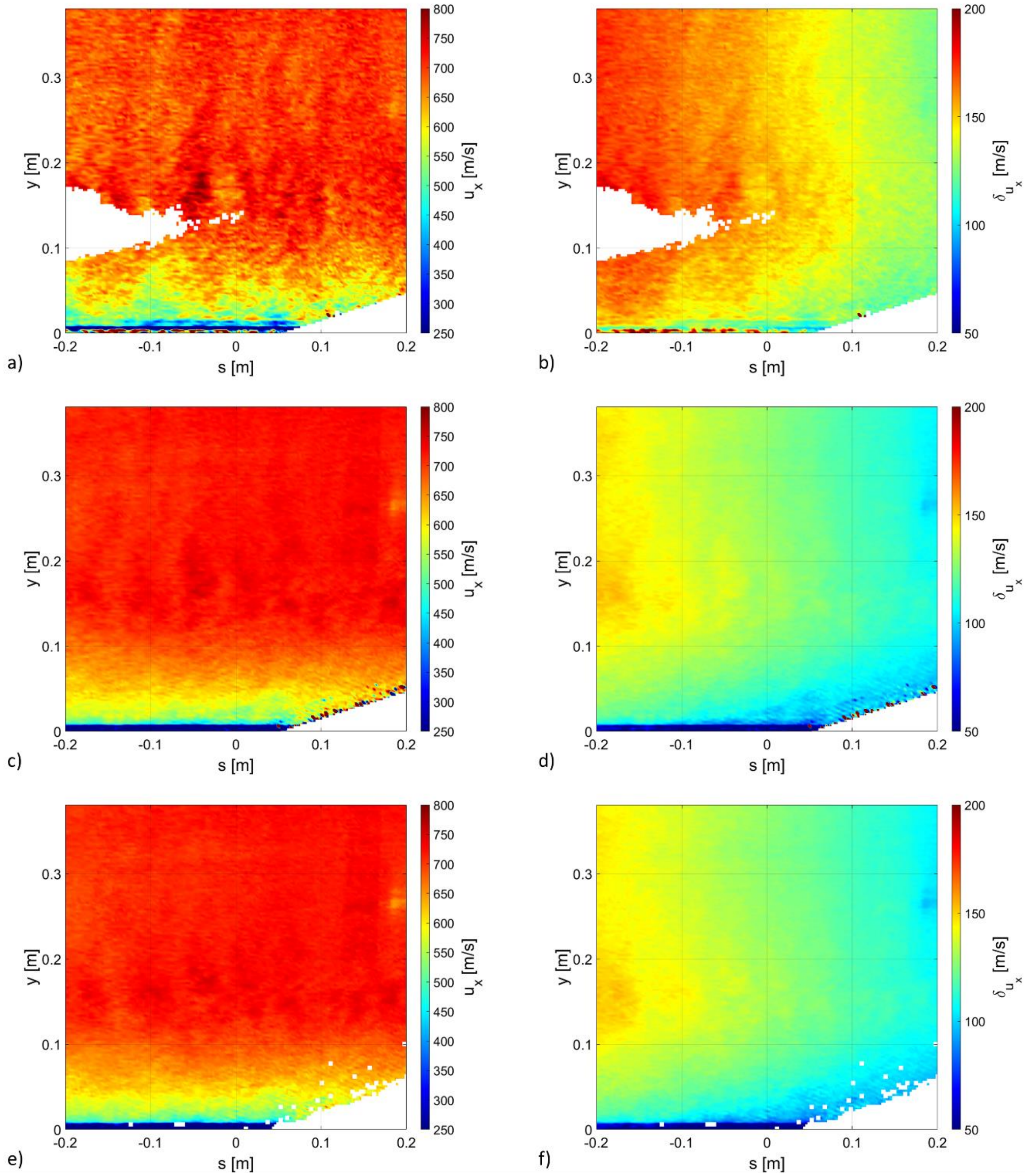

Figure A9. Uncertainty in streamwise velocity in freestream/boundary layer. a) velocity from standard evaluation, b) uncertainty from standard evaluation, c) velocity from COS evaluation, d) uncertainty from COS evaluation, e) velocity from COS + SS evaluation, and f) uncertainty from COS + SS evaluation. White regions contain no valid data.

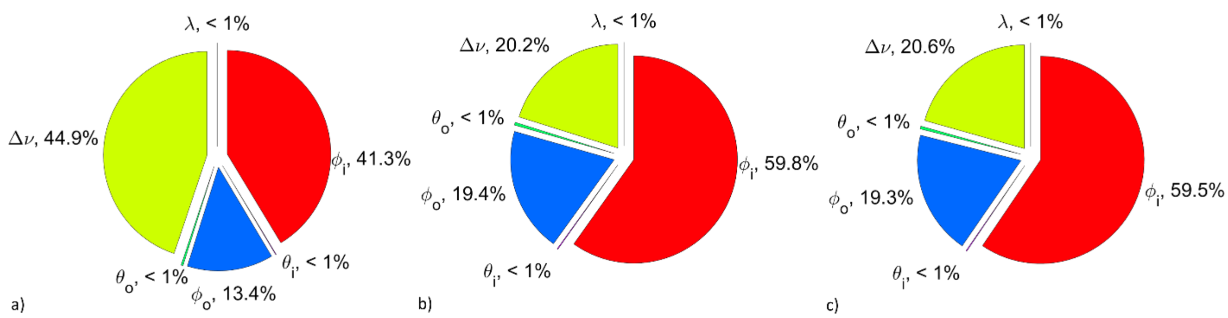

Figure A10. Distribution of uncertainties. a) standard evaluation, b) COS evaluation, and c) COS + SS evaluation.

Acknowledgments

The authors would like to thank the tunnel staff at the NASA Langley 4-Foot Unitary Plan Wind Tunnel for their help and cooperation in completing these tests. Additional thanks are given to Jim Ross for his continuing support of these research efforts. Funding for this work was through the NASA Aerosciences Evaluation and Test Capabilities (AETC) Portfolio and the NASA Transformational Tools and Technologies (TTT) program, Innovative Measurements discipline.

References

[1] Slotnick, J., Khodadoust, A., Alonso, J., Darmofal, D., Gropp, W., Lurie, E., and Mavriplis, D., "CFD Vision 2030 Study: A Path to Revolutionary Computational Aerosciences," *NASA CR-2014-218178*.

[2] Jackson, C.M., Corlett, W.A., and Monta, W.J., "Description and Calibration of the Langley Unitary Plan Wind Tunnel," *NASA TP-1905*, 1981.

[3] Hollis, B.R., Berger, K.T., Berry, S.A., Brauckmann, G.J., Buck, G.M., DiFulvio, M., Horvath, T.J., Liechty, D.S., Merski, N.R., Murphy, K.J., Rufer, S.J., and Schoenenberger, M., "Entry, Descent, and Landing Aerothermodynamics: NASA Langley Experimental Capabilities and Contributions," *AIAA 52nd Aerospace Sciences Meeting*, January 2014, National Harbor, MD.

[4] Ross, J.C., Denison, M., Childs, R. Garcia, J., Stremel, P., Hawke, V., Spooner, H., Robinson, P., Reed, M., Kleb, W.L., Watkins, N., Danehy, P.M., Burns, R., and Fahringer, T., "Evaluation of CFD for Simulation of High-Supersonic Control-Surface Effectiveness," *AIAA Aviation 2021 Forum*, August 2021, Virtual Event.

[5] Garcia, J.A., Brown, J.L., Kinney, D.J., Bowles, J.V., Huynh, L.C., Jiang, X.J., Lau, E. and Dupzyk, I.C., "Co-Optimization of Mid Lift to Drag Vehicle Concepts for Mars Atmospheric Entry," *10th AIAA/ASME Joint Thermophysics and Heat Transfer Conference*, June 2010, Chicago, IL.

[6] Fahringer, T.W., Burns, R.A., Danehy, P.M, Bardet, P.M., and Felver, J., "Pulse-Burst Cross-Correlation Doppler Global Velocimetry," *AIAA Journal*, Vol. 58, No. 6, June 2020, pp. 2364-2369.

[7] Cadel, D.R., and Lowe, K.T., "Cross-Correlation Doppler Global Velocimetry (CC-DGV)," *Optics and Lasers in Engineering*, Vol. 71, Aug. 2015, pp. 51-61.

[8] Burns, R.A., Fahringer, T.W., and Danehy, P.M., "Velocity measurements across and oblique shock using pulse-burst cross-correlation DGV," *AIAA Scitech 2021 Forum*, January 2021, Virtual Event.

[9] Childs, R. Stremel, P., Hawke, V., Garcia, J., Kleb, W.L., Hunter, C., Parikh, P., Patel, M.K., Alter, S.J., Rhode, M.N., and Salarai, K., "Flow Characterization of the NASA Langley Unitary Plan Wind Tunnel, Test Section 2: Computational Result," *AIAA Aviation 2021 Forum*, August 2021, Virtual Event.

[10] Meyers, J.F., "Development of Doppler Global Velocimetry as a Flow Diagnostics Tool," *Measurement Science and Technology*, Vol. 6, No. 6, 1995, pp. 769-783

[11] Danehy, P.M., Wisser, B.M., Fahringer, T.W., Winski, C.S., Falman, B.E., Shea, S., Boyda, M., and Lowe, K.T., "Laser Light Sheet Flow Visualization of the Space Launch System Booster Separation Test," *AIAA Aviation 2019 Forum*, Dallas, TX, 2019.
[12] Tsai, R., "A versatile camera calibration technique for high-accuracy 3D machine vision metrology using off-the-shelf TV cameras and lenses," *IEEE Journal on Robotics and Automation*, Vol. 3, No. 4, pp. 323-344, 1987.
[13] Forkey, J.N., Lempert, W.R., and Miles, R.B., "Corrected and calibrated I2 absorption model at frequency-doubled Nd:YAG laser wavelengths," *Applied Optics*, Vol. 36, No. 27, pp. 6729-6738.
[14] Baldwin, A., Mears, L.J., Kumar, R., and Alvi, F.S., "Effects of Reynolds Number on Swept Shock-wave/Boundary-Layer Interactions," *AIAA Journal*. Vol. 59, No. 10, pp. 3883-3899, 2021.
[15] Zhang, Z., "A flexible new technique for camera calibration," *IEEE Transactions on Pattern Analysis and Machine Intelligence*, Vol. 22, No. 11, pp. 1330-1334.